

1 **Importance of multiple sources of iron for the upper ocean** 2 **biogeochemistry over the northern Indian Ocean**

3 Priyanka Banerjee¹

4 ¹Divecha Centre for Climate Change, Indian Institute of Science, Bangalore, India.

5 *Correspondence to:* Priyanka Banerjee (pbanerjee@iisc.ac.in)

6

7 **Abstract**

8 Although the northern Indian Ocean (IO) is globally one of the most productive regions and receives dissolved
9 iron (DFe) from multiple sources, there is no comprehensive understanding of how these different sources of DFe
10 can impact upper ocean biogeochemical dynamics. Using an Earth system model with an ocean biogeochemistry
11 component this study shows that atmospheric deposition is the most important source of DFe to the upper 100 m
12 of the northern IO, contributing more than 50% of the annual DFe concentration. Sedimentary sources are locally
13 important in the vicinity of the continental shelves and over the southern tropical IO, away from high atmospheric
14 depositions. While atmospheric depositions contribute to more than 10% (35%) to 0-100 m (surface level)
15 chlorophyll concentrations over large parts of the northern IO, sedimentary sources have similar contribution to
16 chlorophyll concentrations over the southern tropical IO. Such increases in chlorophyll are primarily driven by an
17 increase in diatom population over most of the northern IO. The regions that are susceptible to chlorophyll
18 enhancement following external DFe additions are where low levels of background DFe and high background
19 [nitrate-to-iron](#) values are observed. Analysis of DFe budget over selected biophysical regimes over the northern
20 IO points to vertical mixing as the most important mechanism for DFe supply, while the importance of advection
21 (horizontal and vertical) varies seasonally. Apart from removal of surface DFe by phytoplankton uptake,
22 subsurface balance between DFe scavenging and regeneration is crucial in replenishing DFe pool to be made
23 available to surface layer by physical processes.

24 **1 Introduction**

25 Iron is an essential micronutrient for primary producers in the ocean due to the catalytic role of iron in
26 photosynthesis, respiration, and nitrogen fixation (Geider & La Roche, 1994; Raven, 1988). Although iron is one
27 of the most abundant elements in the Earth's crust (McLennan, 2001), its low solubility (Sholkovitz et al., 2012)
28 coupled with an intricate balance between complexation by ligands and high scavenging tendency does not make
29 it readily bioavailable (Boyd & Ellwood, 2010). It has been estimated that iron availability limits primary
30 productivity in as much as ~30% of the global oceans, which results in accumulation of unutilized macronutrients
31 like nitrate and phosphate (Moore et al., 2013a). Even in regions experiencing nitrate limitation of productivity,
32 nitrogen fixation is controlled by the supply of iron (e.g., Mills et al., 2004; Moore et al., 2009; Schlosser et al.,
33 [2014](#)). [Several artificial iron addition experiments performed in the open oceans have demonstrated its](#)
34 [significance in regulating phytoplankton growth \(e.g., Boyd et al., 2007; Coale et al., 1996; de Baar et al., 2005;](#)
35 [Yoon et al., 2018\)](#), while natural iron fertilizations have also shown high levels of carbon export from the upper
36 [ocean following increased productivity \(e.g., Blain et al., 2007; Pollard et al., 2009\)](#).

37 The main external sources of dissolved iron (DFe) to the world oceans are atmospheric depositions (e.g., Conway
38 et al., 2014; Jickells et al., 2005), continental sediments (Elrod et al., 2004; Johnson et al., 1999), river inputs (e.g.,
39 Buck et al., 2007; Canfield, 1997), sea ice (Sedwick & DiTullio, 1997; Wang et al., 2014) and iron seeping from
40 hydrothermal vents (e.g., Nishioka et al., 2013; Tagliabue et al., 2010). Most ocean biogeochemistry models
41 simulating the iron cycle estimate dust ($1.4\text{--}32.7 \text{ Gmol yr}^{-1}$) or sedimentary sources ($0.6\text{--}194 \text{ Gmol yr}^{-1}$) to have
42 the highest contribution to ocean DFe inventory (Tagliabue et al., 2016). However, many of these models do not
43 include hydrothermal sources of DFe. Numerical modelling using dust, sedimentary and hydrothermal sources of
44 DFe have shown that while ocean column DFe inventory is most sensitive to sedimentary and hydrothermal DFe,
45 atmospheric and sedimentary sources of DFe have the largest impact on atmospheric carbon dioxide (Tagliabue
46 et al., 2014). This is because while atmospheric and sedimentary DFe can impact productivity over both the open
47 and coastal oceans, iron from hydrothermal vents reaching the surface water depends on deepwater ventilation
48 and stabilizing impact of organic ligands (Tagliabue et al., 2010; Sander and Koschinsky, 2011). However, with
49 availability of more *in situ* DFe measurements, the relative importance of different sources of DFe are being re-
50 examined at global as well as regional scales.

51 The northern Indian Ocean (IO) is one of the most productive regions of the global oceans, contributing high
52 levels of organic carbon fluxes to the deeper ocean (e.g., Barber et al., 2001; Madhupratap et al., 2003; Rixen et
53 al., 2019). The monsoonal winds drive phytoplankton blooms over different regions of the northern IO, arising
54 from distinct physical mechanisms in different seasons. These mechanisms include blooms due to coastal and
55 open ocean upwelling, advection of nutrients by ocean currents, and mixed layer deepening by winter convection.
56 Episodic blooms are also triggered by passage of cyclones (Kuttippurath et al., 2021) and mesoscale eddies
57 (Prasanna Kumar et al., 2004; Vidya & Prasanna Kumar, 2013). The region hosts one of the most intense oxygen
58 minimum zones of the world oceans (Schmidtko et al., 2017) and is globally one of the major denitrification sites
59 (e.g., Morrison et al., 1999; Bianchi et al., 2012). Several water column measurements have shown that the primary
60 limiting nutrient over the northern IO is reactive nitrogen with possible colimitation by silicate (Košić et al., 2009;
61 Moore et al., 2013a; Morrison et al., 1998). In recent years, a few studies using ocean biogeochemistry models
62 have also pointed to possible iron limitation of phytoplankton blooms during southwest monsoon months (June-
63 September), especially over upwelling regions of the western Arabian Sea (AS), which is the north-western part
64 of the IO (Košić et al., 2009; Wiggert et al., 2007). These findings on the role of iron limitation have also been
65 supported by incubation experiments over the AS during the late southwest monsoon, which have noted
66 chlorophyll enhancements following iron enrichments (Moffett et al., 2015). Furthermore, *in situ* measurements
67 during the late southwest monsoon have revealed complete drawdowns of silicate, owing to its high utilization
68 under iron limitation, as well as high nitrate-to-iron ratios over the western AS (Naqvi et al., 2010). Nutrient
69 enrichment experiments over the central AS during northeast monsoon months (December-March) have also
70 revealed signatures of iron and nitrate colimitation, with addition of these two nutrients supporting increases in
71 diatoms and coccolithophores (Takeda et al., 1995). Colimitation by nitrogen, phosphorus and iron has been
72 identified over the southern Bay of Bengal (BoB, the north-eastern part of the IO) and the eastern equatorial IO
73 (Twining et al., 2019). Thus, availability of iron can have major impacts on availability of other macronutrients
74 and productivity, which can in turn impact denitrification and mid-depth oxygen levels in this region by
75 modulating fluxes of sinking organic matters.

76 In general, there is a reduction in surface DFe concentrations over the northern IO from north to south. Systematic
77 DFe measurements, encompassing all seasons over the AS, conducted during the Joint Global Ocean Flux Study
78 (JGOFS) of the 1990s showed DFe concentrations often exceeding 1 nM, especially during the southwest
79 monsoon (Measures & Vink, 1999). Subsequent measurements revealed lower levels of DFe with surface values
80 ranging between 0.2-1.2 nM over the AS and between 0.2-0.5 nM over the BoB (Chinni et al., 2019; Chinni &
81 Singh, 2022; Grand et al., 2015; Moffett et al., 2015; Vu & Sohrin, 2013). These values are generally higher than
82 most of the open ocean regions. In contrast, southwards of the equatorial IO have surface DFe values generally
83 less than 0.2 nM (e.g., Chinni et al., 2019; Grand et al., 2015; Twining et al 2019; Vu & Sohrin, 2013). The oxygen
84 minimum zone, located to the north of the equator between depths of 150-1000 m, has elevated levels of DFe (>1
85 nM), possibly due to DFe transport from reducing shelf sediments and remineralization of sinking organic matter
86 (Moffett et al., 2007).

87 The overall high values of DFe over the northern IO can stem from multiple external sources of DFe identified
88 within this region: atmospheric aerosol inputs (dust and black carbon) from South and Southwest Asia (Banerjee
89 et al., 2019; Srinivas et al., 2012), continental shelf sediments, high river discharge, especially, over the BoB (e.g.,
90 Chinni et al., 2019; Grand et al., 2015) and hydrothermal vents from the Central Indian Ridge that mainly impact
91 DFe levels at depths of around 3000 m (Nishioka et al., 2013). The importance of episodic dust depositions in
92 alleviating iron limitations of primary productivity over the central AS has been identified, during the northeast
93 monsoon when a deeper ferricline compared to the nitracline yields a high nitrate-to-iron ratio (Banerjee and
94 Kumar, 2014). Additionally, modelling studies over the AS have demonstrated that DFe derived from dust
95 deposition can support about half of the observed primary productivity and a large fraction of nitrogen fixation
96 (Guieu et al., 2019). Centennial-scale model simulations over the IO have revealed that changes in phytoplankton
97 community structure have resulted in increased (reduced) carbon uptake over the eastern (western) IO in response
98 to increased anthropogenic DFe deposition in the present day compared to pre-industrial levels (Pham & Ito,
99 2021). Yet another challenge is that, away from regions with high aerosol loading, other sources of DFe can
100 become important in supporting ocean productivity and controlling patterns of nutrient limitations. Such
101 understanding of relative roles of different sources of DFe in controlling the biogeochemical dynamics of the
102 northern IO remains unexplored. This is important considering the multiple sources of DFe over the northern IO.
103 To this end, the present study uses a suite of simulations from a state-of-the art Earth system model with an iron
104 cycle in its ocean biogeochemistry component to explore the relative contribution of different sources of DFe to
105 phytoplankton blooms and impacts on nutrient availability over the upper 100 m of the northern IO. Furthermore,
106 DFe budget has been analysed over the upper ocean for varied biophysical regimes in this region to identify how
107 different sources of DFe can impact the total DFe budget.

108

109 **2 Data and model**

110 The study uses satellite and reanalysis products, ocean observation data, and an Earth system model to assess
111 contributions of different sources of DFe to phytoplankton blooms over the northern IO. For the present study,
112 the northern IO is considered to encompass 30°N–20°S latitude, 40°–105°E longitude. Thus, the tropical part of
113 the southern IO is also included. Only the open ocean regions, having bottom depth greater than 1000 m, are
114 studied here. The four seasons referred to in this study are defined as: the northeast monsoon: December-March;

115 spring intermonsoon: April-May; southwest monsoon: June-September; and fall intermonsoon: October-
116 November.

117 **2.1 Model**

118 This study uses the ocean component Parallel Ocean Program version 2 (POP2) (Smith et al., 2010) embedded in
119 the Community Earth System Model (CESM) version 2.1. This version of CESM incorporates several
120 improvements over previous versions of the model (Danabasoglu et al., 2020). The POP2 model is a level-
121 coordinate model having Arakawa B-grid in the horizontal with North Pole displaced over Greenland. The vertical
122 resolution is 10 m for the upper 160 m and decreases with depth to 250 m in the bottom. The horizontal resolution
123 is nominally 1° with meridional resolution increasing to 0.27° near the equator (Danabasoglu et al., 2012),
124 implying that mesoscale eddies are not resolved. Momentum advection is based on a second-order central
125 advection scheme while tracer advection relies on a third-order upwind advection scheme. Vertical ocean mixing
126 is parameterized using the non-local K-Profile parameterization (Large et al., 1994), which is incorporated into
127 CESM2.1 via the Community Ocean Vertical Mixing (CVMix) framework. Horizontal mixing is parameterized
128 using the Gent and Williams (1990) scheme, which includes eddy-induced velocity in addition to diffusion of
129 tracers along isopycnals. Macronutrients and oxygen are initialized from World Ocean Atlas 2013 version 2
130 dataset (Garcia et al., 2014a, b) and alkalinity is initialized using GLObal Ocean Data Analysis Project
131 (GLODAPv2; Olsen et al., 2016). Temperature and salinity are initialized from January-mean values from the
132 Polar Science Center Hydrographic Climatology, which is based on data from Levitus et al. (1998). Ecosystem
133 tracers, including iron, chlorophyll, dissolved organic and inorganic carbon are initialized from a previous CESM1
134 simulation.

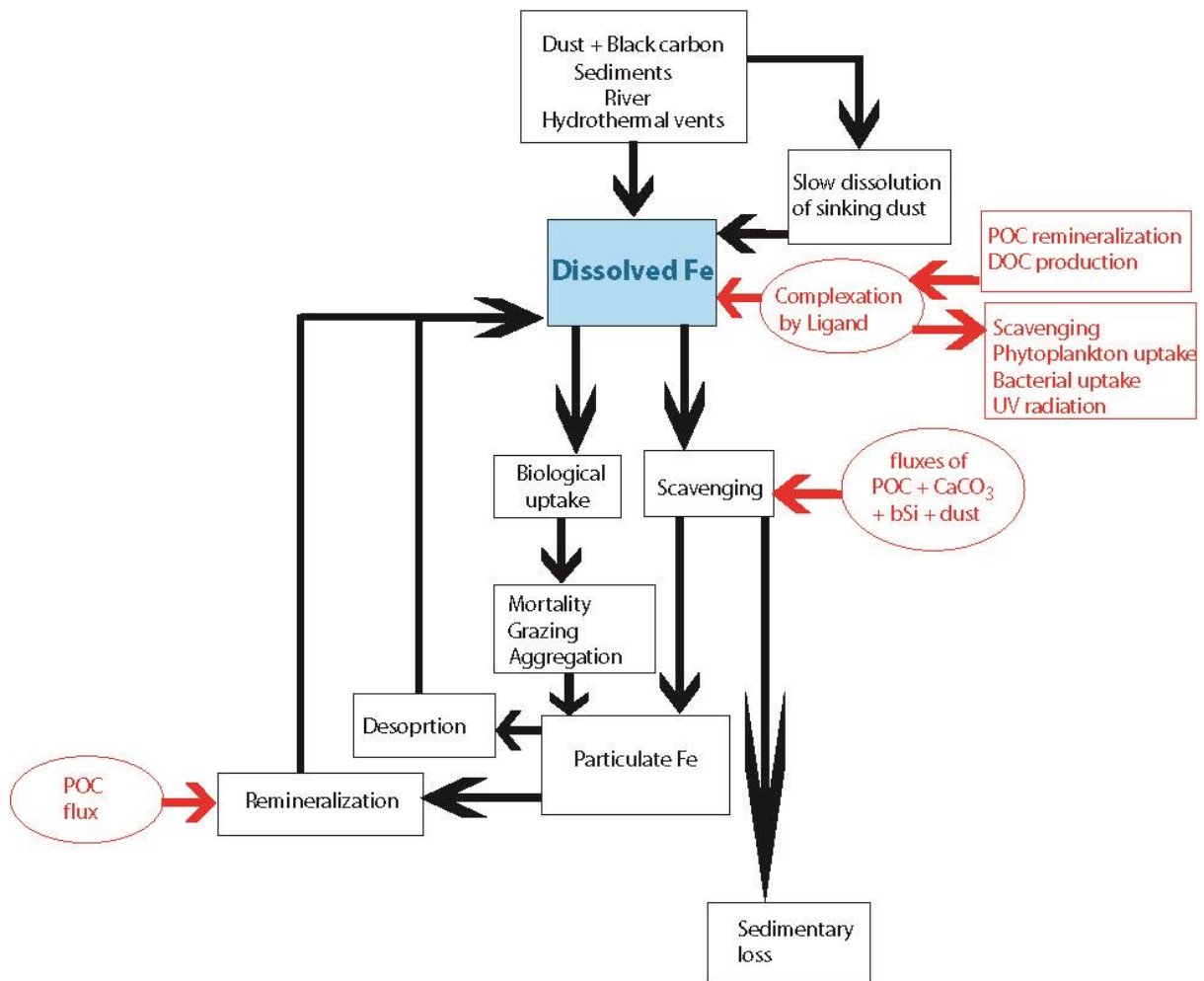
135 The biogeochemistry component of POP2 is implemented using Marine Biogeochemistry Library (MARBL),
136 which is the most updated version of the previously implemented Biogeochemistry Elemental Cycle (BEC) model
137 (Long et al., 2021). The model includes key limiting nutrients (N, P, Si, Fe), three types of explicit phytoplankton
138 functional groups (diatoms, diazotrophs and nano/picophytoplankton), one implicit calcifier group, and one
139 zooplankton type. The C:N ratio for nutrient assimilation is fixed at 117:16 (Anderson and Sarmiento, 1994),
140 whereas P:C, Fe:C, Si:C and chlorophyll:C ratios are allowed to vary based on ambient nutrient concentrations.
141 The Fe:C ratio is allowed to change within a fixed range based on phytoplankton growth terms, loss terms, and
142 the iron uptake half-saturation constant for different phytoplankton groups (Moore et al., 2004). For each of the 3
143 phytoplankton groups the minimum allowed Fe:C ratio is 2.5 $\mu\text{mol mol}^{-1}$. The maximum allowed Fe:C ratio is 30
144 $\mu\text{mol mol}^{-1}$ for diatoms and small phytoplankton, and 60 $\mu\text{mol mol}^{-1}$ for diazotrophs due to their higher demand
145 for iron. The zooplankton Fe:C ratio is fixed at 3.0 $\mu\text{mol mol}^{-1}$. Individual nutrient limitation for phytoplankton is
146 assessed based on Michaelis-Menten nutrient uptake kinetics, which is a function of the specific nutrient
147 concentration and nutrient uptake half-saturation coefficient. The half-saturation coefficient is nutrient-specific
148 and phytoplankton-group specific. Nutrient limitation terms vary from 0 to 1, with 0 being the most limiting
149 nutrient. Multiple nutrient limitation follows Liebig's law of minimum, so that the nutrient limitation term with
150 minimum value limits phytoplankton growth rate (Long et al., 2021). Loss of phytoplankton in MARBL is
151 accounted for by grazing, mortality, and aggregation of sinking flocculants.

152 The main DFe sources considered in MARBL are atmospheric depositions, shelf sediments, riverine inputs, and
153 hydrothermal vents (Fig. S1). Globally, these sources of DFe account for 13.62 Gmol yr⁻¹, 19.68 Gmol yr⁻¹, 0.37
154 Gmol yr⁻¹, and 4.91 Gmol yr⁻¹, respectively (Long et al., 2021). Atmospheric sources of DFe are from dust and
155 black carbon depositions obtained from a fully coupled CESM2 simulation in hindcast mode at nominal 1° spatial
156 resolution as a part of the Coupled Model Intercomparison Phase 6 (CMIP6) contribution. Dust emissions and
157 transport/deposition are calculated, respectively, using the Community Land Model version 5 (CLM5) and
158 Community Atmosphere model version 6 (CAM6) in Whole Atmosphere Community Climate Model (WACCM)
159 configuration. The newly included Modal Aerosol Module version 4 (MAM4) in CAM6 includes dust in the
160 accumulation and coarse modes. Black carbon is emitted in the primary mode and transferred to accumulation
161 mode via aging (Liu et al., 2016). Monthly climatology of dust and black carbon for the year 2000 is used in
162 repeating mode. About 3.5% of dust is assumed to be iron with the solubility of iron depending on the ratio
163 between coarse and fine dust fluxes. This accounts for increasing iron solubility with increasing distance from
164 dust source regions. A constant solubility of 6% is assigned to iron derived from black carbon aerosols. In addition
165 to surface iron release, there is slow dissolution of sinking “hard” dust fraction (~98% of total dust) with depth
166 such that ~0.3% of dust will dissolve over 4000 m (Armstrong et al., 2002; Moore et al., 2004). For the rest of the
167 2% “soft” dust, remineralization takes place with a length-scale of 200 m. Sedimentary iron supply is based on
168 sub-grid scale bathymetry that depends on two factors: firstly, for reducing sediments, it is proportional to
169 particulate organic carbon fluxes in regions where these fluxes are larger than 3 g C m⁻² yr⁻¹; secondly, in oxic
170 sediments, it depends on constant low background fluxes and bottom current velocity, which accounts for
171 sediment resuspension. As a result, the main sources of sedimentary DFe are along continental shelves and
172 productive margins, with little contribution coming from the deep ocean. For the river source of DFe, discharge
173 data for the year 2000 from Global Nutrient Export from WaterSheds (GlobalNEWS, Mayorga et al., 2010) is
174 combined with constant DFe concentration of 10 nM. For hydrothermal vents, a constant flux of iron from the
175 grid boxes containing vents is applied so that the total hydrothermal vent iron flux is equal to approximately 5.0
176 Gmol yr⁻¹.

177 Iron input to the ocean is balanced by losses from biological uptake and scavenging. The biological uptake of iron
178 is based on the species-specific Fe:C ratio, which varies based on ambient DFe concentration, as discussed
179 previously. The biological uptake term also includes routing of phytoplankton iron to zooplankton based on its
180 feeding preference. Losses of iron from the biological pools are through mortality, aggregation, grazing upon
181 phytoplankton by zooplankton, as well as higher trophic grazing on zooplankton (Long et al., 2021). The
182 scavenging loss of DFe is expressed as a two-step process similar to the thorium scavenging model: involving the
183 calculation of the net adsorption rate to sinking particles and modification of this rate by the ambient iron
184 concentration (Moore and Braucher, 2008). The total sinking particles consist of particulate organic carbon,
185 biogenic silica, calcium carbonate, and dust, which strongly influence DFe scavenging in excess of ligand
186 concentrations. The particulate organic carbon is multiplied by 6 to account for the non-carbon portion of the
187 organic matter that can take part in scavenging. In CESM, scavenging increases non-linearly with DFe
188 concentration. About 90% of the scavenged iron enters the sinking particulate pool, while the rest is lost to
189 sediments. Along with the scavenging contribution, iron released from grazing and mortality of autotrophs and
190 zooplankton also enters the particulate iron pool. Remineralization of this sinking particulate iron replenishes DFe
191 and is parameterized as a function of sinking particulate organic carbon flux. This results in maximum

192 remineralization taking place within the upper 100 m where particulate organic carbon flux is the highest.
193 Additionally, slow desorption of sinking particulate iron also releases DFe at depths and is calculated using a
194 constant desorption rate of $1.0 \times 10^{-6} \text{ cm}^{-1}$ for particulate iron. The model also includes an explicit ligand tracer
195 for complexing Fe, with ligand sources being from particulate organic carbon remineralization and dissolved
196 organic matter production. Ligand sinks involve scavenging, uptake by phytoplankton, ultraviolet radiation, and
197 bacterial uptake or degradation (Long et al., 2021). An overview of the different sources and sinks of DFe used
198 in CESM-MARL is given in Figure 1.

199 ~~Iron input to oceans is balanced by losses from biological uptake and scavenging. Loss of iron from the biological~~
200 ~~pool occurs through mortality and grazing upon phytoplankton by zooplankton as well as higher trophic grazing~~
201 ~~on zooplankton. In CESM, scavenging increases non-linearly with DFe concentration. The scavenging rate~~
202 ~~depends on the total sinking fluxes of particulate organic carbon, biogenic silica, calcium carbonate and dust,~~
203 ~~which strongly influence DFe in excess of ligand concentrations (Moore and Braucher, 2008). Scavenged iron~~
204 ~~enters the particulate iron pool, while iron released from grazing and mortality of autotrophs and zooplankton also~~
205 ~~contributes to the particulate iron pool depending on species specific Fe:C ratios. Remineralization of particulate~~
206 ~~iron at depth is parameterized as a function of the particulate organic carbon flux. Desorption of iron contributes~~
207 ~~to the remineralized iron pool and is calculated using a constant desorption rate for scavenged iron. In addition,~~
208 ~~there is slow dissolution of “hard” dust fraction (~98% of total dust) with depth such that ~0.3% of dust will~~
209 ~~dissolve over 4000 m (Armstrong et al., 2002; Moore et al., 2004). For the remainder of the 2% “soft” dust,~~
210 ~~remineralization takes place with a length scale of 200 m. The model also includes an explicit ligand tracer for~~
211 ~~complexing Fe, with ligand sources being from particulate organic carbon remineralization and dissolved organic~~
212 ~~matter production. Ligand sinks are scavenging, uptake by phytoplankton, ultraviolet radiation, and bacterial~~
213 ~~uptake or degradation.~~



214

215 **Figure 1: Schematic representation of iron cycle in the ocean component of the CESM model. The texts/boxes/arrows**
 216 **in black show the main processes affecting the dissolved iron pool, while those in red further show what controls the**
 217 **processes impacting the dissolved iron pool. POC (DOC): particulate (dissolved) organic carbon, bSi: biogenic silica.**

218

219 This study is based on 5 sets of simulations for identifying contributions from different sources of DFe: control
 220 simulation (CTRL); and simulations that individually remove DFe supply from atmospheric depositions (NATM),
 221 sediments (NSED), rivers (NRIV) and hydrothermal vents (NVNT). Differences between CTRL and NATM
 222 simulations indicate the biogeochemical impacts solely due to atmospheric deposition of DFe and is referred to
 223 as ATM. Similarly, biogeochemical impacts solely from sedimentary, river and hydrothermal DFe sources are,
 224 respectively, referred to as SED, RIV and VNT cases. Simulations have been conducted in hindcast mode for 60
 225 years using forcing from the Coordinated Ocean-ice Reference Experiments version 2 (CORE-II) dataset for the
 226 years 1948-2007 (Large & Year, 2009). The CORE-II data includes interannual variability and consists of 6-
 227 hourly temperature, air density, specific humidity, 10 m wind-speeds, and sea-level pressure from National
 228 Centers for Environmental Prediction/ National Center for Atmospheric Research (NCEP/NCAR) Reanalysis
 229 (Kalnay et al., 1996). Daily shortwave and longwave radiation are taken from Goddard Institute for Space Studies-
 230 International Satellite Cloud Climatology Project radiative flux profile data (GISS-ISCCP-FD) (Zhang et al.,
 231 2004). Monthly precipitation is combined Global Precipitation Climatology Project (GPCP, Huffman et al., 1997)
 232 and Climate Prediction Center Merged Analysis of Precipitation (CMAP, Xie & Arkin, 1997) data. Monthly

233 [streamflow since 1948 used in this study has been previously derived from gauge data, where linear regression](#)
234 [was also employed using CLM3 model streamflow to fill-in missing data \(Dai et al., 2009\).](#) The present study
235 uses the last 10 years of simulations, given its focus on impacts of DFe sources on biogeochemistry of the upper
236 100 m of the oceans at seasonal scale.

237 **2.2 Observation data**

238 Monthly climatology for ocean temperature, salinity and nutrients have been obtained from World Ocean Atlas
239 2018 (WOA18) at 1°x1° spatial resolution (Garcia et al., 2019). Monthly surface chlorophyll concentrations have
240 been obtained from the European Space Agency Ocean Color Climate Change Initiative (OC-CCI) version 5 at 4
241 km spatial resolution for the period 2003-2020 (Satyendranath et al., 2019). OC-CCI merges ocean color
242 information from multiple sensors: Moderate Resolution Imaging Spectroradiometer (MODIS, 2002-present),
243 Sea-Viewing Wide Field-of-View Sensor (SeaWiFS, 1997-2010), MEdium Resolution Imaging Spectrometer
244 (MERIS, 2002-2012) and Visible Infrared Imaging Radiometer (VIIRS, 2012-present). The product is bias-
245 corrected and quality-controlled, yielding much lower data gaps compared to individual sensors. Monthly
246 climatology of mixed layer depth (MLD) gridded at 1°x1° spatial resolution has been obtained from Argo profiles
247 based on a hybrid algorithm that calculates a suite of MLDs using several criteria, such as gradient/threshold
248 method, maxima or minima of a particular property, intersection with seasonal thermocline (Holte et al., 2017).
249 The resulting patterns are analysed to yield final MLD estimates. To explore ocean surface circulation, Ocean
250 Surface Current Analysis Real-time (OSCAR) data at 0.33°x0.33° spatial resolution and 5-day temporal resolution
251 has been used. Horizontal velocities are measured using sea surface heights, ocean surface winds, and sea surface
252 temperatures, thereby accounting for flows due to geostrophic balance, Ekman dynamics, and thermal wind
253 (Dohan & Maximenko, 2010).

254

255 To examine the ability of CESM to realistically simulate the variation in DFe concentrations in the upper 100 m
256 over the northern IO, this study uses DFe profile compilations by Tagliabue et al. (2012) and the GEOTRACES
257 Intermediate Data Product 2021 (Schlitzer et al., 2021). To these, published data from Moffett et al. (2015) has
258 also been added, comprising DFe data collected in the AS during September 2007. The DFe estimated in these
259 data are based on filtration of seawater through filter sizes between 0.2-0.45 µm.

260

261 **3 Results and discussions**

262 First, the performance of CESM-POP2 simulations with respect to observations over the northern IO is examined.
263 Next, the contributions of different DFe sources to upper ocean DFe concentrations, phytoplankton blooms and
264 patterns of nutrient limitations is discussed. Finally, the paper explores how different sources of DFe can influence
265 the total DFe budget across selected biophysical regimes over the northern IO.

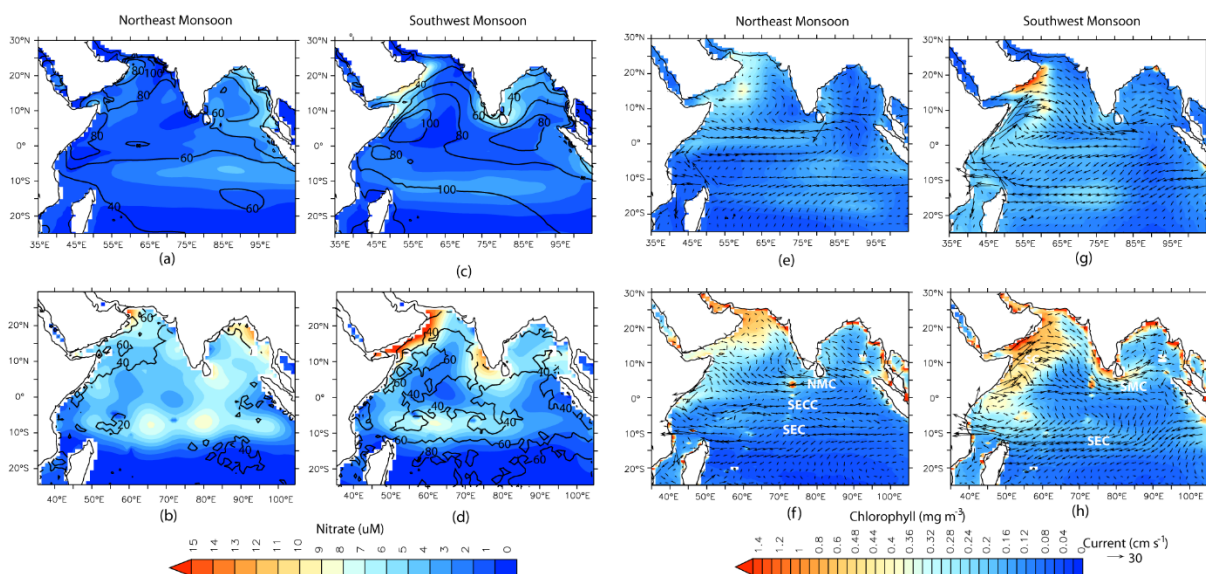
266

267 **3.1 Model evaluation**

268 In this section CESM simulation (for CTRL case) of physical parameters as well as nitrate and chlorophyll
269 concentrations over the upper 100 m of the northern IO is evaluated. Except for MLD, ocean currents, and
270 chlorophyll, all modeled parameters have been compared with WOA18 observations. Simulated MLDs are
271 compared with Argo-based values of Holte et al. (2017), ocean currents are compared with OSCAR data, and

272 chlorophyll concentrations are compared with OC-CCI observations. In general, CESM shows good
 273 correspondence with observations of seasonal cycle of temperature, salinity and MLD. However, there is positive
 274 temperature and salinity bias over IO (Figs. S2 and S3 in the Supplement). This warm bias over IO differs from
 275 the previous version of CESM, which has a cold bias in this region (Danabasoglu et al., 2020). Figure 2 shows
 276 seasonal climatology in CESM simulations and observations, for MLD, nitrate concentrations, surface ocean
 277 currents, and chlorophyll concentrations. Overall, CESM simulates the main features of surface ocean circulation
 278 and spatio-temporal variations in MLD well. There are some deviations, such as a much stronger simulated Somali
 279 Current along the northeast coast of Africa, especially during the southwest monsoon season, which can lead to
 280 strong advection of upwelled nutrients away from this region. CESM also simulates a stronger South Equatorial
 281 Current during southwest monsoon, which occupies a broader region compared to observations and leads to a
 282 stronger westward flow in the model between 0-5°S latitude. The net result of the warm and positive salinity bias
 283 is that CESM simulates much deeper MLD than observations throughout the year across the study domain.
 284 Averaged annually, the largest overestimation (of ~40 m) is over the equatorial IO particularly during the spring
 285 and fall intermonsoon months, when the Wyrki Jet is prevalent over the region (Figs. S3 e-f). Additionally, MLD
 286 overestimation of ~45 m is also seen over the AS during February-March and the southern tropical IO during
 287 September-October, both associated with winter-convection.

288 With respect to the seasonal cycle of nitrate, CESM has the least bias over AS followed by BoB (Figs. 2a-d and
 289 S4), but its performance is comparatively lower over the equatorial IO and southern tropical IO. For example,
 290 WOA18 data shows the highest value of nitrate over southern tropical IO in January, whereas in CESM simulation
 291 the highest nitrate concentration is shifted to April-June associated with mixed layer deepening. On the other
 292 hand, CESM simulates a much weaker seasonal cycle of nitrate over the equatorial IO compared to WOA18
 293 observations. These regions, over southern tropical IO and the equatorial IO, where CESM fares poorly also have
 294 fewer nutrient profile observations compared to AS and BoB. For example, no more than 10 nitrate observations
 295 are available in a grid-point over the southern tropical IO and equatorial IO, whereas there are several grid-points
 296 over the AS where more than 30 observations are available. Overall, CESM simulations underestimate nitrate
 297 with respect to WOA18 data for the upper 100 m of the water column.



298

299 **Figure 2: Comparison of CESM-CTRL simulated variables (upper panels) with observations (lower panels) for**
300 **northeast monsoon (a,b,e,f) and southwest monsoon (c,d,g,h). Shading in (a-d) are nitrate concentrations averaged for**
301 **upper 100 m and the black contours are the mixed layer depth (m). Shading in (e-h) are surface chlorophyll**
302 **concentrations and the vectors are the surface currents. SEC: South Equatorial current, SECC: South Equatorial**
303 **Counter Current, NMC: Northeast Monsoon Current, SMC: Southwest Monsoon Current, SC: Somali Current.**

304

305 Turning to chlorophyll concentrations, CESM simulations capture the main characteristics of the seasonal cycle
306 and its spatial distribution over the northern IO (Figs. 2e-h and S4), with certain biases and shifts in the timing of
307 the peak blooms. For example, over the BoB, the model has difficulty in capturing the temporal evolution of
308 chlorophyll concentrations. Over the AS and the equatorial IO, peak bloom in the simulations occurs in September,
309 in contrast to July in the observations. Similarly, over the southern tropical IO, the peak bloom is delayed in the
310 model to October as compared to its appearance in July in observations. Most of the AS and the BoB show
311 underestimation ($\sim -60\%$) in simulated chlorophyll concentration with respect to OC-CCI values. Such
312 underestimation of major nutrients and chlorophyll over most of the northern IO are common to many modelling
313 studies where coastal regimes and mesoscale processes are not adequately captured without finer spatial resolution
314 (e.g., Dutkiewicz et al., 2012; Ilyina et al., 2013; Long et al., 2021; Moore et al., 2013b; Pham & Ito, 2021). For
315 example, a modelling study by Resplandy et al. (2011) has shown that eddy-induced vertical transport is
316 responsible for $\sim 40\%$ of nitrate fluxes in the winter convection regions of the AS during the late northeast
317 monsoon. The study also showed that mesoscale eddies can account for 65-91% of vertical and lateral advection
318 of nitrate in the upwelling regions of the AS during the southwest monsoon. Additionally, the positive MLD bias
319 simulated by CESM can trigger light limitation of phytoplankton growth, leading to underestimation of
320 chlorophyll. If the threshold depth for photosynthesis is considered as the depth of the isolume given by 0.415
321 $\text{mol quanta m}^{-2} \text{d}^{-1}$ ($Z_{0.145}$, Boss & Behrenfeld, 2010; Letelier et al., 2004), then the CESM simulated MLD is
322 deeper than the $Z_{0.145}$, leading to light limitation of phytoplankton growth over the entire AS and large parts of
323 BoB throughout the year (Fig. S5). During the southwest monsoon, almost the entire domain experiences light
324 limitation, especially off the coast of Somalia and the southern tropical IO.

325 CESM simulations of DFe are evaluated next, using all available *in situ* DFe concentration data for upper 20 m
326 of the ocean, for different seasons. In addition, distribution of DFe along selected transects for the upper 100 m
327 are studied: (1) CLIVAR cruise 109N along the eastern IO during April 2007; and (2) GEOTRACES cruises GI-
328 01, GI-02, [GI-03](#), GI-04 and GI-05. While CESM simulates the general pattern of DFe distribution over the
329 northern IO reasonably well, DFe variation with depth and with increasing distance from the coast is stronger in
330 simulations than in observations. For upper 20 m, [Pearson product-moment correlation coefficient calculated](#)
331 [between observed and simulated DFe concentrations is 0.62](#) (Figs. 3a-d). The coefficients for correlation between
332 observed and simulated DFe for GEOTRACES and CLIVAR transects vary between 0.64 and 0.38 (Fig. 3e). [All](#)
333 [these correlation coefficients are significant at 95% confidence level based on Student's t-test with n-2 degrees of](#)
334 [freedom, where n is the sample size.](#) This indicates that CESM is able to reproduce the north-to-south gradient in
335 DFe concentrations, the comparatively low DFe concentration west of 65°E over the AS, as well as increases in
336 DFe with depth over both the eastern and western IO reasonably well. [Overall, CESM simulates positive bias in](#)
337 [DFe concentration over the study domain \(see Table S1\). A closer look at the pattern of bias in simulated DFe](#)
338 [reveals several features: \(1\) the magnitude of the positive bias is much lower to the south of \$5^\circ\text{S}\$ latitude compared](#)
339 [to the north. \(2\) CESM simulated DFe has low magnitude of negative bias to the west of \$60^\circ\text{E}\$ longitude over the](#)

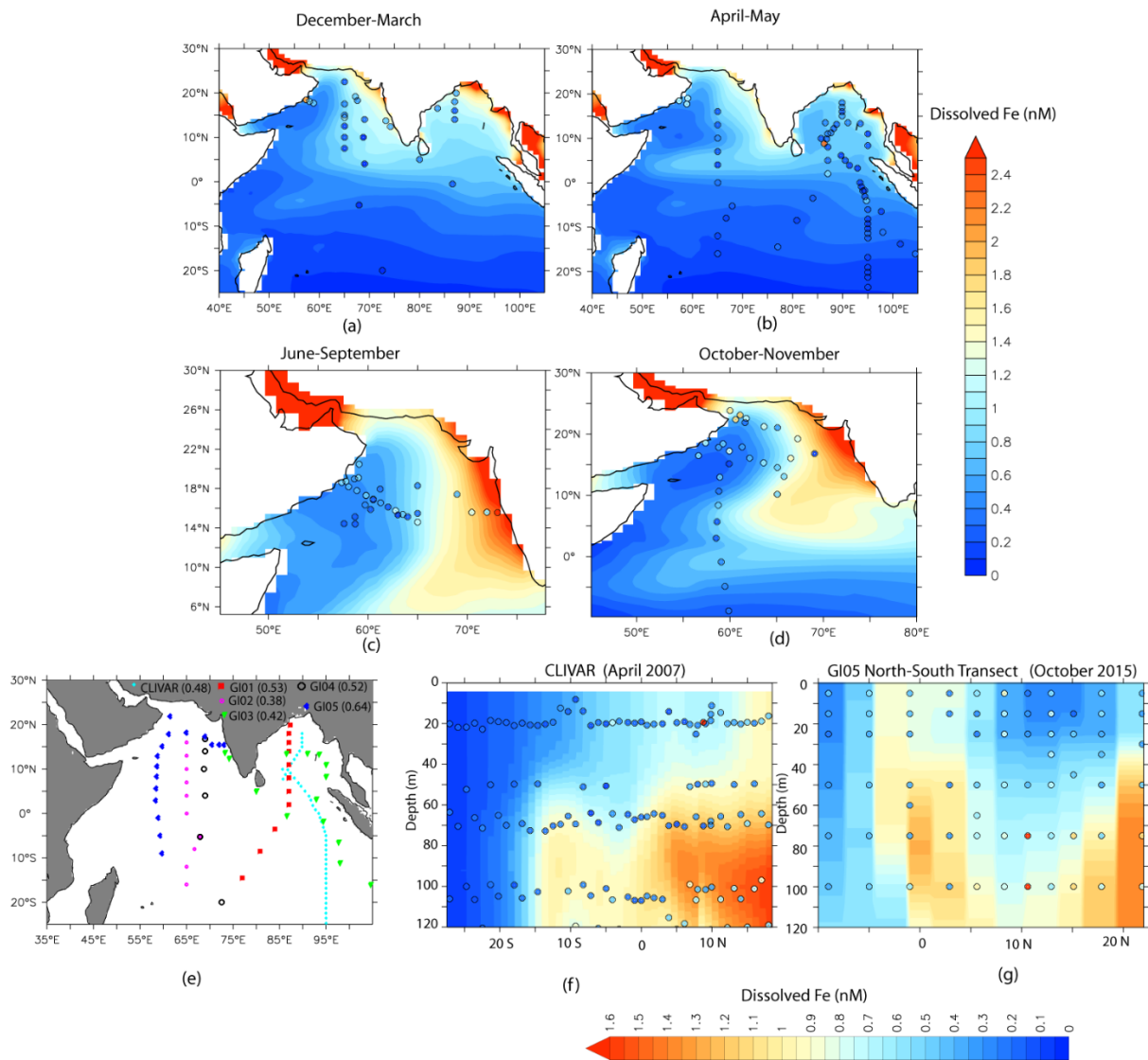
340 AS near the dust sources and (3) Coastal and open oceans experience similar magnitudes of positive DFe bias
341 throughout the domain, implying that DFe bias might be stemming from multiple sources.

342 Figures 3 f and g show two examples of variation of DFe distribution with latitude and depth along the eastern
343 and western IO, respectively. The model overestimates DFe values, especially to the north of the equator and at
344 depths greater than 60 m. Such overestimation of DFe over the northern IO in CESM could result from a variety
345 of factors, like source strength, assumed solubility of iron, and uncertainties in the removal of DFe by biological
346 uptake as well as scavenging. With respect to source strength, dust deposition is one possible factor that can lead
347 to overestimation of simulated DFe. Using Dust Indicators and Records of Terrestrial and MARine
348 Palaeoenvironments (DIRTMAP) version 2 database of modern day dust deposition (Kohfeld & Harrison, 2001)
349 an attempt has been made here to understand CESM bias in dust deposition over AS. Median dust deposition
350 values from DIRTMAP ranges between $\sim 14 \text{ g m}^{-2}\text{yr}^{-1}$ over the western AS (40° - 60° E), $\sim 7 \text{ g m}^{-2}\text{yr}^{-1}$ over the central
351 AS (60° - 70° E) and $\sim 20 \text{ g m}^{-2}\text{yr}^{-1}$ over the eastern AS (70° - 80° E) (Kohfeld & Harrison, 2001). Corresponding
352 median values of dust deposition over these locations from CESM model are $5 \text{ g m}^{-2}\text{yr}^{-1}$, $9 \text{ g m}^{-2}\text{yr}^{-1}$ and $14 \text{ g m}^{-2}\text{yr}^{-1}$
353 respectively, indicating a general underestimation of dust deposition by CESM, especially to the west of 60° E
354 longitude. Over the eastern IO, using mixed layer dissolved Al concentrations dust depositions have been
355 estimated to be 0.2 - $3.0 \text{ g m}^{-2}\text{yr}^{-1}$ between 20° S to 10° N latitude (Grand et al., 2015). In a separate study, based on
356 Al concentrations in the aerosol, Srinivas and Sarin (2013) have estimated dust dry-deposition flux of 0.3 - $3.0 \text{ g m}^{-2}\text{yr}^{-1}$
357 over BoB. Dust deposition from CESM is on the lower end of this range varying from $1.1 \text{ g m}^{-2}\text{yr}^{-1}$ over
358 the northern BoB to $0.2 \text{ g m}^{-2}\text{yr}^{-1}$ near the equator. Sediment traps deployed at shallow depths over the BoB have
359 recorded annual lithogenic fluxes varying from the northern to the southern bay as $\sim 15 \text{ g m}^{-2}\text{yr}^{-1}$ ($\sim 89.5^{\circ}$ E, 17.5° N)
360 to $\sim 4 \text{ g m}^{-2}\text{yr}^{-1}$ (87° E, 5° N) (Unger et al., 2003). The corresponding variations in CESM dust deposition are $\sim 9 \text{ g m}^{-2}\text{yr}^{-1}$,
361 to $\sim 2 \text{ g m}^{-2}\text{yr}^{-1}$. Thus, overall, there is some underestimation of dust deposition over the northern IO, which
362 might not explain positive DFe bias in CESM simulations. However, there is a possibility of fractional solubility
363 of Fe from dust having an impact on DFe derived from atmospheric sources. Over the AS, percentage solubility
364 of aerosol has been reported to vary between 0.02 and 0.43% (Srinivas et al., 2012). Considering that Fe constitutes
365 3.5% of dust by weight and using 0.02% and 0.5% as the lower and upper bounds to Fe solubility, the total fluxes
366 of soluble Fe based on CESM dust deposition are calculated. The calculated iron flux ranges from 0.002 (0.04)
367 $\mu\text{mol m}^{-2} \text{ d}^{-1}$ over the western AS to 0.01 (0.35) $\mu\text{mol m}^{-2} \text{ d}^{-1}$ over the eastern AS for 0.02% (0.5%) solubility. The
368 corresponding ranges of soluble Fe flux from CESM is $0.05 \mu\text{mol m}^{-2} \text{ d}^{-1}$ in the west to $0.8 \mu\text{mol m}^{-2} \text{ d}^{-1}$ in the
369 eastern AS. Again, using median dust deposition values from DIRTMAP data and assuming 0.5% iron solubility,
370 soluble Fe fluxes vary from 0.12 to $0.17 \mu\text{mol m}^{-2} \text{ d}^{-1}$ from west to east AS. It is therefore clear that CESM model
371 input of soluble Fe from atmosphere is overestimated compared to observations. This inference does not change
372 even after adding the contribution of black carbon (after assuming 6% solubility of Fe) to the atmospheric iron
373 flux. This is because fractional solubility of Fe in CESM varies from 1.2% over northwestern AS to $\sim 5\%$ over the
374 southern AS. Ship-based measurements, on the other hand, have observed that high levels of CaCO_3 in the dust
375 over the AS acts as a neutralizing agent, leading to much lower aerosol solubility (Srinivas et al., 2012).
376 Additionally, for the GI05 transect (Fig. 3g), DFe concentration reduces drastically in the NATM case (Fig. S6 a-
377 c), indicating that dust deposition and its solubility is the major factor contributing to the simulated levels of DFe
378 and its biases.

379 The impact of dust solubility on DFe concentration, however, does not explain the positive biases in simulated
380 DFe over the BoB. The percentage solubility of aerosol iron measured over the BoB is high, varying between
381 2.3% and 24%, due to presence of acid species from anthropogenic activities (Srinivas et al., 2012). This leads to
382 much higher soluble iron deposition than that is obtained from CESM. For example, in CESM the soluble Fe flux
383 over BoB varies from ~0.05 to 0.35 $\mu\text{mol m}^{-2} \text{d}^{-1}$, whereas, calculated soluble Fe flux varies from 0.06 to above 1
384 $\mu\text{mol m}^{-2} \text{d}^{-1}$. Thus, atmospheric supply of iron is possibly underestimated over the BoB. It is, therefore, quite
385 possible that this positive bias in DFe stems from either sedimentary or river sources. In fact, comparing CTRL
386 simulation with NATM and NSED along the CLIVAR transect in Figure 3f, reveals considerable contribution of
387 sedimentary sources of DFe, especially at depth greater than 60 m (Fig. S6 d-f). Furthermore, the latitudinal
388 change in salinity along this transect closely follows the latitudinal pattern of change in DFe from NATM case,
389 but not DFe from NSED case. To examine this, DFe from NATM and NSED cases and salinity from CTRL case
390 have been taken along the CLIVAR transect from depths greater than 60 m and have been detrended. The
391 correlation between DFe from NATM and salinity is -0.75 indicating that non-atmospheric sources of DFe is
392 associated with fresher water transported from the coastal regions. The corresponding correlation between DFe
393 from NSED and salinity is -0.16 indicating that non-sedimentary sources of DFe has no salinity dependence. The
394 underestimation of atmospheric iron deposition along with salinity-dependence of DFe from the NATM case
395 together indicates that enhanced transport of sediments from continental margins is likely to be the source of DFe
396 bias along the CLIVAR transect. One possible explanation is that the low resolution of the model is unable to
397 capture the high velocity of the coastal currents that may limit the spreading of sediments from the coastal regions
398 to the open oceans. The simulated coastal current is weaker than OSCAR observations during April, when the
399 CLIVAR measurements were undertaken (Fig. S6 g-h). This can lead to greater diffusive spreading of iron from
400 the coast into the open ocean. Such an effect of model resolution has been previously shown to result in a higher
401 sedimentary contribution to DFe off the northwest Pacific and southwest Atlantic ocean (Harrison et al., 2018).

402

403



404

405 **Figure 3:** Comparison of CESM-CTRL simulated DFe (shading) with the observations (filled circles) compiled from
 406 various cruises. The spatial distribution maps in (a-d) consider season-wise DFe distribution averaged over the upper
 407 20 m. (e) The different cruise tracks from which DFe measurements have been used are marked. The numbers within
 408 the parentheses are the correlation coefficients between observed and simulated DFe for each cruise. The vertical
 409 transects in (f-g) show DFe gradients in the water column over (f) the eastern Indian Ocean and (g) the western Indian
 410 Ocean.

411 With respect to loss terms, biases in Fe uptake and scavenging can impact simulated DFe concentrations,
 412 especially in the surface waters. To account for Fe uptake by phytoplankton, particulate organic carbon export
 413 fluxes at 100 m calculated from ^{234}Th fluxes have been used in conjunction with Fe:C ratios. Since the cellular
 414 Fe:C ratio varies widely depending on external DFe availability and phytoplankton species composition, a lower
 415 bound of $6 \mu\text{mol mol}^{-1}$ and an upper bound of $50 \mu\text{mol mol}^{-1}$ have been considered. The lower bound is based on
 416 measurements over the eastern IO (Twining et al., 2019) where oligotrophic conditions are encountered. The
 417 upper bound is based on measurements over the tropical North Atlantic where high dust deposition leading to
 418 high surface DFe concentration prevails (Twining et al., 2015). Combining Fe:C values with particulate organic
 419 carbon export fluxes from JGOFS cruises (Buesseler et al., 1998) yields Fe uptake by phytoplankton varying
 420 between ~ 0.0004 and $\sim 0.0035 \mu\text{mol m}^{-3} \text{d}^{-1}$ for all seasons over the AS. Phytoplankton Fe uptake from CESM
 421 over the AS varies between ~ 0.0001 and $\sim 0.002 \mu\text{mol m}^{-3} \text{d}^{-1}$, which are on the lower end of observation-based

422 values. Over the BoB, phytoplankton Fe uptake varies between ~ 0.00002 and $\sim 0.004 \mu\text{mol m}^{-3} \text{d}^{-1}$ based on
423 available POC measurements (Anand et al., 2017; 2018). The corresponding ranges of CESM simulated DFe
424 uptake are ~ 0.0002 to $\sim 0.001 \mu\text{mol m}^{-3} \text{d}^{-1}$, which is within the range of values calculated from observations. With
425 respect to scavenging losses, based on particulate Fe value from the eastern tropical South Pacific and ^{234}Th fluxes
426 over the AS, Chinni and Singh (2022) estimated abiotic removal of $0.001\text{-}0.005 \mu\text{mol m}^{-3} \text{d}^{-1}$ for the upper 100 m.
427 In the present simulations, average scavenging removal is $\sim 0.003 \mu\text{mol m}^{-3} \text{d}^{-1}$ over both the AS and BoB (range:
428 0.002 to $0.026 \mu\text{mol m}^{-3} \text{d}^{-1}$) and reduces to less than $0.001 \mu\text{mol m}^{-3} \text{d}^{-1}$ to the south of the equator. Overall, Fe
429 uptake by phytoplankton is possibly underestimated over the AS, which can contribute to some overestimation of
430 DFe in the surface waters over this region. Over BoB, Fe uptake is within the range of observation-based values.
431 Scavenging removal simulated by CESM is also within the range of observation-based values and is possibly not
432 contributing to DFe bias in CESM.

433
434 ~~It is seen that CESM consistently overestimates dissolved oxygen over the northern IO with respect to the WOA18~~
435 ~~concentrations (Fig. S5). This implies that overestimation of sub-surface DFe concentrations in the model does~~
436 ~~not originate in the magnitude and the spatial extent of poorly oxygenated sub-surface waters responsible for~~
437 ~~increased remineralization of particulate iron. The impact of organic ligands in maintaining DFe stock by~~
438 ~~preventing scavenging losses can introduce yet another notable source of bias in simulated DFe. Only one study~~
439 ~~has measured ligand concentrations over the northern IO, during the spring intermonsoon of 1995 (Witter et al.,~~
440 ~~2000). At 100 m depth, observed ligand concentration ranges from 1.47 nM over the western AS to 4.94 nM over~~
441 ~~the eastern AS. The corresponding values from CESM simulations range from 1.55 nM in the western AS to 1.19~~
442 ~~nM over the eastern AS. However, it is not possible to conclude about the impact of ligands on simulated DFe~~
443 ~~biases based on a single study. With respect to scavenging losses, it is quite possible that underestimation of~~
444 ~~productivity over the northern IO can lead to corresponding bias in scavenging losses. This is because the base~~
445 ~~scavenging rate in CESM, apart from depending on dust fluxes, is also a function of sinking fluxes of particulate~~
446 ~~organic matter, biogenic silica, and calcium carbonate. For example, averaged over a year, there is $\sim 60\%$~~
447 ~~underestimation in CESM of surface chlorophyll concentrations over the northern IO, which would impact the~~
448 ~~sinking fluxes of biogenic matter. This can reduce scavenging losses, especially, when there is a likely~~
449 ~~underestimation of dust deposition by CESM. Underestimation of phytoplankton biomass over the northern IO~~
450 ~~can also lead to underestimation of phytoplankton uptake losses of DFe in the upper 100 m, which can be yet~~
451 ~~another source of overestimation of DFe.~~

452 To summarize, the ocean component of CESM has deeper MLD than observations, underestimates nitrate and
453 chlorophyll, and overestimates DFe concentrations. Together, this can result in weaker iron-limitation in the
454 simulations compared to observations. Over the AS, the positive bias in simulated DFe is present mostly to the
455 east of 60°E longitude and can be related to the higher solubility of atmospheric iron in CESM compared to the
456 observations. Over the BoB, DFe bias likely originates from enhanced transport of sedimentary iron from
457 continental shelf margins. To the west of 60°E , simulated DFe has negative bias of low magnitude, possibly
458 because underestimation of dust deposition is counterbalanced by overestimation of iron-solubility. Over the
459 southern tropical IO, the magnitude of bias is also low compared to the rest of the study domain. Still, the model
460 simulates spatial and temporal patterns of ocean physical features, as well as variations in chlorophyll

461 concentrations, nitrate, and DFe concentrations over the northern IO reasonably well. This gives confidence in
462 using the model to study the iron cycle over the region. Taking the above understanding of strengths and
463 shortcomings of the model into account, the importance of different DFe sources with respect to biogeochemistry
464 of the upper 100 m of the northern IO is explored next.

465

466 3.2 Contribution of multiple iron sources

467

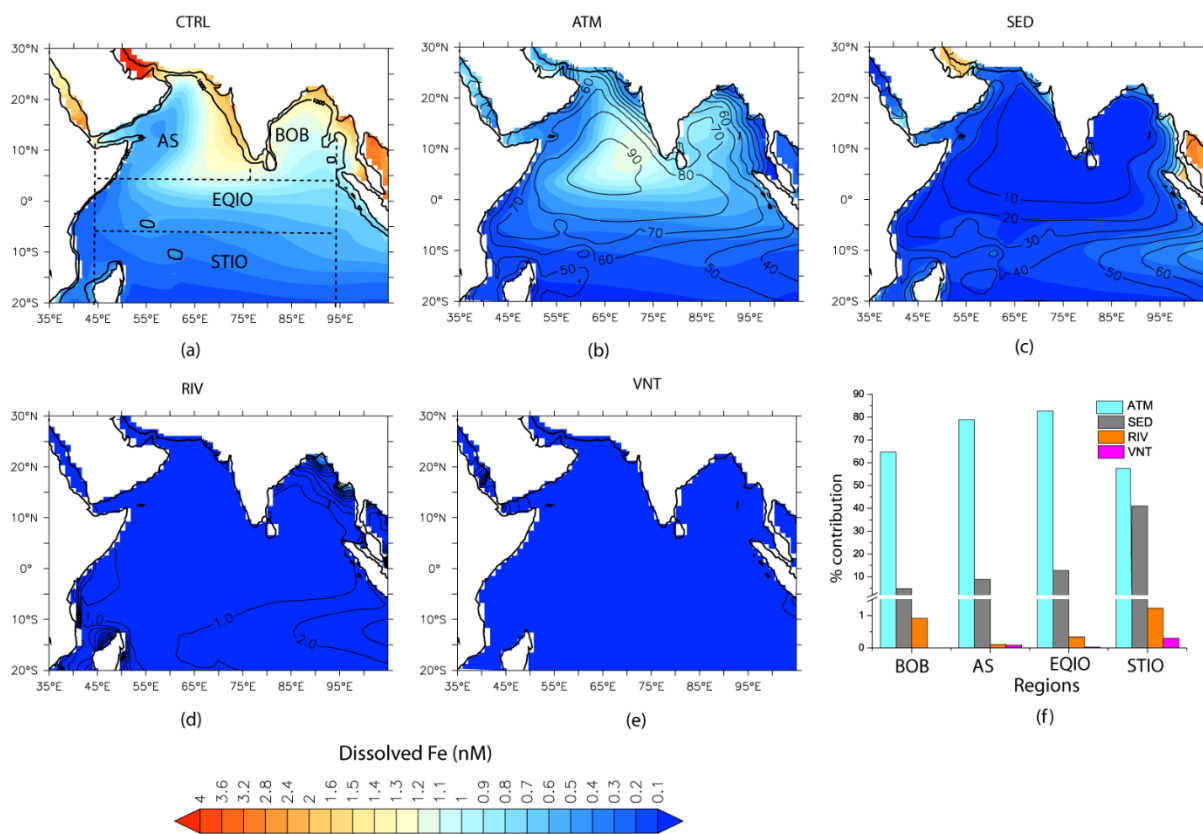
468 Figure 4 summarizes the contributions of different sources to annually averaged DFe concentration. Source-wise
469 DFe contributions for northeast and southwest monsoons are shown in Figs. S7 and S8, respectively. Overall, the
470 relative contribution from different sources to DFe is nearly the same across different seasons, except for the
471 somewhat higher contribution of atmospheric DFe during southwest monsoon compared to northeast monsoon.
472 This is because the arid and semi-arid regions surrounding the northern IO experiences maximum dust activity
473 from late spring to early southwest monsoon months (e.g., Banerjee et al., 2019; Léon and Legrand, 2003). In the
474 annual average, atmospheric deposition is the most important source of DFe over the northern IO and contributes
475 well above 50% of the total DFe concentrations (ATM case in Fig. 4b). Furthermore, atmospheric deposition
476 contributes more than 70% of DFe supply over most of the AS, southern BoB, and the equatorial IO. The location
477 of the intertropical convergence zone during northeast monsoon (~10°S latitude) determines the southern limit of
478 the influence of atmospheric deposition because southwards of the intertropical convergence zone there is a rapid
479 reduction in DFe concentrations. Dust is the predominant contributor to the atmospheric deposition flux of iron.
480 Over the northern AS, dust is mostly transported from Iran, Pakistan, Afghanistan, and the Arabian Peninsula,
481 whereas over southern AS dust from north-eastern Africa also becomes important (Jin et al., 2018; Kumar et al.,
482 2020). Over northern and southern BoB, the major sources of dust are the Indo-Gangetic Plain and northeast
483 Africa, respectively (Banerjee et al., 2019). Eastwards of 90°E, black carbon contributes ~50% to atmospheric
484 DFe flux during the northeast monsoon (not shown). The source of black carbon in this region is biomass burning
485 and fossil fuel combustion transported from the Indo-Gangetic Plain and Southeast Asia (Gustafsson et al., 2009;
486 Moorthy & Babu, 2006).

487 The second largest source of DFe is from continental shelf sediments (Fig. 4c), which become dominant in the
488 vicinity of the shelves. High sedimentary sources of DFe are characteristic of the Andaman Sea where incoming
489 rivers can contribute $\sim 600 \times 10^6 \text{ T yr}^{-1}$ of sediments (Robinson et al., 2007). It has been estimated that terrestrial
490 sources contribute more than 80% to total organic carbon in the inner shelf region of the Gulf of Martaban,
491 adjacent to the Andaman Sea (Ramaswamy et al., 2008). Elsewhere, sedimentary contributions of ~20% to overall
492 DFe are found in CESM runs along the northern part of west coast of India and the eastern BoB. Within Ganga-
493 Brahmaputra system, which is responsible for discharge of $\sim 11 \times 10^8 \text{ T yr}^{-1}$ of sediments, only 10% of sediments
494 is estimated to be transported longshore, with most of the sediments accumulating within the shelf and
495 subterranean canyon (Liu et al., 2009). Over the open ocean, sedimentary sources are most important within 10°-
496 15°S latitude where the South Equatorial Current is responsible for ~50% of DFe supply via advection from the
497 Indonesian shelf. During southwest monsoon, sedimentary contribution by the South Equatorial Current extends
498 farther westward (~70°E longitude, Fig. S8c) compared to the northeast monsoon (~80°E longitude, Fig. S7c).
499 Signatures of elevated AI due to sedimentary contribution is seen in ship-borne measurements (Grand et al., 2015;

500 Singh et al., 2020). In fact, such measurements have shown that the South Equatorial Current separates DFe-rich
501 oxygen-poor water of the northern IO from the DFe-poor oxygen-rich water of the southern tropical IO (Grand et
502 al., 2015).

503 River sources contribute negligibly to total DFe concentrations (Fig. 4d), except in the immediate vicinity of the
504 mouths of large river systems in the northeast BoB: the Ganges-Brahmaputra and the Irrawady-Sittang-Salween.
505 This can arise from the fact that DFe from river is mostly concentrated within the fresher upper 30 m of the water
506 column to the north of 21°N over the BoB and also due to high scavenging losses of iron at the river mouth.
507 flocculation at the river mouth can quickly lead to near complete losses of DFe compared to other metals (Flegal
508 et al., 1991; Sholkovitz, 1978). Hydrothermal vents also contribute negligibly to DFe concentrations in the upper
509 100 m (Fig. 4e). The hydrothermal vents supplying DFe (often excess of 1.5 nM) in the northern IO are located
510 in the Central Indian Ridge and the Carlsberg Ridge (Chinni & Singh, 2022; Nishioka et al., 2013; Vu & Sohrin,
511 2013), and largely influence DFe concentrations below 1000 m depths. The shallowest hydrothermal plumes
512 enriched with Fe are located between ~650-900 m in the Gulf of Aden (Gamo et al., 2015), overlapping with the
513 depth range at which the Red Sea watermass spreads along the western IO (Beal et al., 2000). Since this watermass
514 occupies progressively deeper depths with distance, sliding underneath Persian Gulf waters, surface DFe values
515 are not impacted by these shallower vents. This is in concordance with simulations of Tagliabue et al. (2010)
516 where, following 500 years of model integration, hydrothermal vents increase globally averaged DFe
517 concentrations by only ~3% in the depth range of 0-100 m.

518 The average contribution of different sources of iron to the upper 100 m is summarized for different open ocean
519 regions over the northern IO in Fig. 4f. Annually averaged atmospheric deposition is clearly the most important
520 source of DFe throughout the northern IO. The exception to the dominant role of atmospheric deposition is the
521 southern tropical IO, where sedimentary sources of iron contribute ~40% to the upper ocean iron budget. Based
522 on the analysis of origin of bias in simulated DFe concentrations in Section 3.1, it is likely that contribution of
523 atmospheric sources to upper 100 m DFe concentration is overestimated over the eastern AS and the contribution
524 of sedimentary sources to upper 100 m DFe concentration is overestimated over the BoB. Averaging over the
525 entire domain, atmospheric source contributes ~67% to the upper 100 m DFe concentration. On masking out the
526 region to the east of 65°E longitude over the AS, where the highest positive bias of DFe from dust has been noted,
527 it is seen that atmospheric source contributes ~65% to the upper 100 m DFe concentration. Again, averaging over
528 the study domain, sedimentary source contributes ~30% to the upper 100 m DFe concentration. On masking out
529 BoB, where positive bias of DFe from sedimentary sources has been identified in Section 3.1, it is seen that
530 sedimentary source contributes ~33% to the upper 100 m DFe concentration. Thus, while biases in the source
531 strength might regionally impact the percentage contribution of DFe from various sources to the northern IO, the
532 overall conclusion of atmospheric source being the most important for upper ocean DFe over the northern IO,
533 followed by sedimentary sources, does not change. River contribution is generally ~1%, with slightly higher
534 contributions in BoB and the southern tropical IO. Hydrothermal vents make negligible contributions throughout
535 the northern IO. Adding these four sources of DFe estimated from CESM experiments does not yield the full
536 100% of the DFe source, owing to non-linear effects associated with iron removal processes as well as
537 complexation by organic ligands.



538
539

540 **Figure 4:** Contribution of different sources of DFe averaged over the year to the total DFe concentrations over the
541 upper 100 m. Shading in (a) shows total DFe concentration with all sources included and shadings in (b-e) shows DFe
542 concentrations arising from individual source. Contours in (b-e) show the percentage contribution of each source to
543 total DFe concentrations. (f) Bar chart depicting source-specific DFe contribution (in %) over Bay of Bengal (BOB),
544 Arabian Sea (AS), equatorial IO (EQIO), and the southern tropical IO (STIO). These regions are marked by the dashed
545 boxes in (a). The thick black contour in (a) traces the 1000 m bathymetry.

546
547
548

3.3 Phytoplankton responses to multiple iron sources

549 In this section, the impact of different sources of DFe on phytoplankton growth is examined. Since river and
550 hydrothermal sources make negligible contributions to the upper ocean iron concentrations, as shown above, these
551 are not considered further.

552 3.3.1 Responses to atmospheric depositions

553 During the northeast and southwest monsoons, atmospheric DFe brings about increases in column-integrated
554 chlorophyll concentrations over most of the northern IO (Figs. 5 a and c). The largest column-integrated positive
555 response is seen in the western AS (west of ~65°E longitude) throughout the year, where atmospheric DFe
556 accounts for more than ~20% of the column-integrated chlorophyll concentration and more than 50% of surface
557 chlorophyll concentration (Fig. S9). This region comes under the influence of upwelling during the southwest
558 monsoon and mixed layer deepening due to winter convection during the northeast monsoon, which can supply
559 macronutrients required for phytoplankton growths (Madhupratap et al., 1996; Morrison et al., 1998). The other
560 region displaying a strong positive response is the southern tropical IO during June-September, where atmospheric
561 DFe contributes ~20% (~35%) of the column (surface) chlorophyll concentration. This is the time of the year
562 when deep mixed layer leads to entrainment of nutrients into the surface layers (Koenig et al., 2009; Lévy et al.,

563 2007). In contrast, there are some regions, like the northern and western AS, the west coast of India and large
 564 parts of the BoB and the eastern IO, which in spite of receiving high atmospheric DFe hardly experience any
 565 chlorophyll response. These regions show <1% increase in column chlorophyll concentrations and generally
 566 coincide with high sedimentary iron input. This is discussed further in Section 3.3.3

567 Species-wise decomposition shows that the increases in chlorophyll during both northeast and southwest
 568 monsoons are driven by increases in diatoms and declines in small phytoplankton (Fig. 6). For example, over the
 569 western AS and southern tropical IO, diatoms increase by at least 40% and small phytoplankton populations
 570 decline by at least 50%. ~~Diatoms outperforming other phytoplankton species has been previously witnessed in *in*~~
 571 ~~*situ* iron fertilization experiments (de Baar et al., 2005). This is due to the large cell size of diatoms enabling~~
 572 ~~higher cellular uptake of iron and also the ability of diatoms for luxury iron uptake, which enables them to~~
 573 ~~outcompete other species in a bloom (Sunda & Huntsman, 1995).~~ An exception is the equatorial IO, where the
 574 positive response of chlorophyll arises from growth of small phytoplankton. In general, this region has very low
 575 levels of macronutrients and is dominated by picoplankton (Vidya et al., 2013). Those regions exhibiting <1%
 576 increase in phytoplankton in response to atmospheric DFe, in contrast, are characterized by proliferation of small
 577 phytoplankton and reductions of diatoms. Although diazotrophs show positive response to atmospheric DFe
 578 addition throughout the region, this group constitutes only ~1% of total phytoplankton biomass.

579 Such differences in species response to external iron addition arise from differences in nutrient uptake between
 580 different phytoplankton functional groups in CESM. Phytoplankton growth rate (μ_i) is parameterized as a product
 581 of resource-unlimited growth rate (μ_{ref} in d^{-1}) at a reference temperature of 30°C, and three terms that describe
 582 nutrient limitation (V_i), temperature dependence (T_f) and light availability (L_i). This is expressed as:

$$583 \mu_i = \mu_{ref} V_i T_f L_i \quad (1)$$

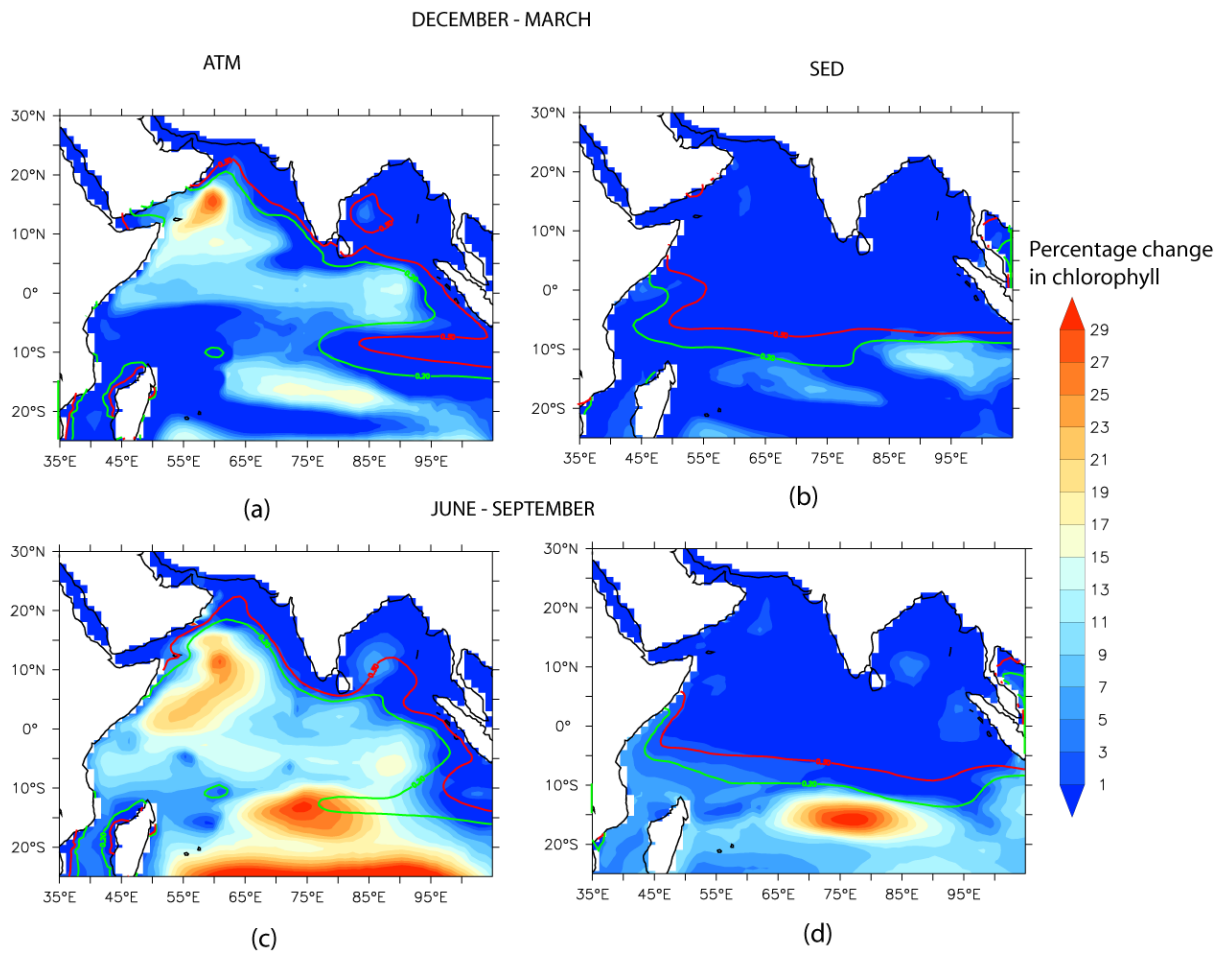
584 The nutrient limitation term for iron, V_i , for a specific phytoplankton group i is expressed as:

$$585 V_i^{Fe} = \frac{Fe}{Fe + K_i^{Fe}} \quad (2)$$

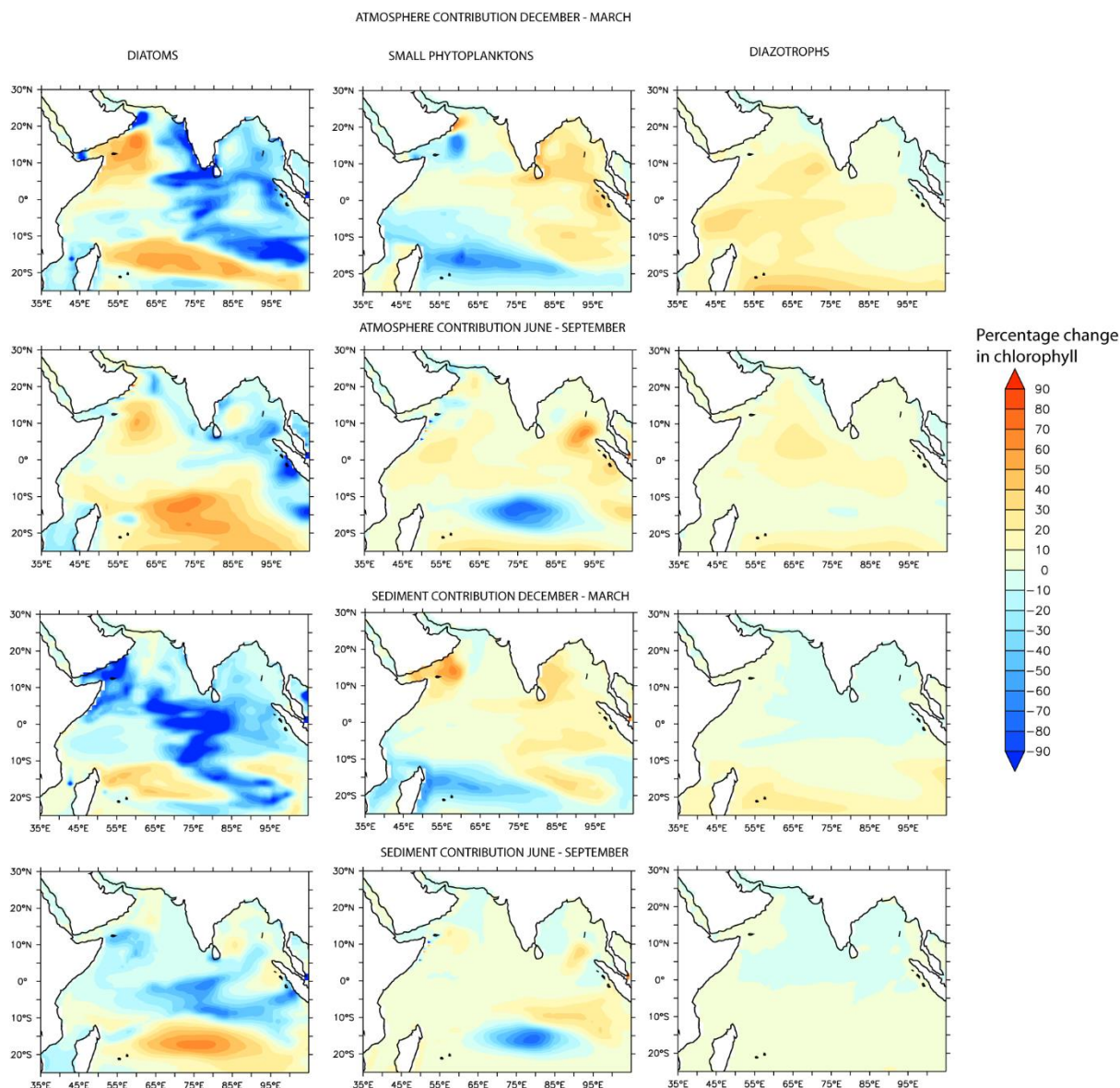
586 where Fe is the concentration of iron and K_i^{Fe} is the Fe uptake half-saturation constant for a phytoplankton group.
 587 While small phytoplankton have been assigned a value of $3.0 \times 10^{-5} \text{ mmol m}^{-3}$ for K_i^{Fe} , diatoms have been
 588 assigned a higher value of $7.0 \times 10^{-5} \text{ mmol m}^{-3}$. This leads to the small phytoplankton outcompeting diatoms when
 589 nutrient levels are low. Additionally, small phytoplankton are subjected to higher grazing pressure than diatoms.
 590 The maximum grazing rate assigned in CESM is 3.3 d^{-1} for small phytoplankton versus 3.15 d^{-1} for diatoms.
 591 Together, the differences in nutrient uptake half-saturation constant and grazing pressure between different
 592 phytoplankton species results in diatom dominating blooms under nutrient-replete conditions.

593 Diatoms outperforming other phytoplankton species has been previously witnessed in *in situ* iron fertilization
 594 experiments along with the existence of a linear relationship between diatom size and iron requirement for growth
 595 (de Baar et al., 2005). Such shifts in phytoplankton community structure in response to DFe additions are also
 596 corroborated by *in situ* experiments over the northern IO. For example, a nutrient addition experiment over the
 597 northern AS during northeast monsoon period has shown that the maximum positive phytoplankton response takes
 598 place due to nitrate+DFe addition (instead of only DFe addition), accompanied by around four-fold increases in
 599 coccolithophores, pennate and large centric diatoms (Takeda et al., 1995). Ship-board iron addition experiments
 600 over the AS during the southwest monsoon resulted in proliferation of visible colonies of haptophyte *Phaeocystis*
 601 *sp.* due to silicate-limitation (Moffett et al., 2015). Over the eastern IO, where both macronutrients and

602 micronutrients are low, nutrient spiking with nitrogen, phosphorus, and iron resulted in increase of
603 Prochlorococcus, Synechococcus, as well as Eukaryotes (Twining et al., 2019).
604



605
606 **Figure 5:** Percentage contribution of (a and c) atmospheric and (b and d) sedimentary sources of iron during (a and b)
607 the northeast monsoon and (c and d) the southwest monsoon to upper 100 m chlorophyll concentrations. Green and
608 red contours show background DFe concentrations of 0.2 nM and 0.3 nM respectively. For the ATM (SED) case,
609 background DFe is obtained from NATM (NSED) simulation.
610



611
 612 **Figure 6:** Species-wise percentage contribution to column chlorophyll (0-100 m) response associated with atmospheric
 613 and sedimentary sources of DFe.

614
 615
 616 **3.3.2 Responses to sedimentary sources of iron**

617 As shown in Fig. 4, sedimentary sources supply less than ~20% of DFe north of ~10°S latitude, whereas between
 618 10°-15°S latitude sedimentary iron can contribute to almost half of the total DFe concentrations. Unlike
 619 atmospheric sources, sedimentary supply of DFe is mostly confined to regions adjoining continental shelves and
 620 islands from where they are introduced to the open ocean by seasonally varying currents. In general, sedimentary
 621 sources make modest contribution to column productivity (<1% of chlorophyll anomalies) to the north of ~10°S
 622 latitude as described above. This is because high dust deposition to the north of the intertropical convergence zone
 623 results in high background DFe concentrations and controls productivity (see also Section 3.3.3). Sedimentary
 624 sources trigger the strongest positive phytoplankton response over the southern tropical IO region during June-
 625 September, where sedimentary DFe advected by the South Equatorial Current can facilitate more than 20%
 626 increase of the upper 100 m chlorophyll concentrations and ~40% increase at the surface. As noted in Section 3.2,

627 although atmospheric deposition contributes nearly half of the total DFe addition to this region, the total iron
628 deposition here is low (<0.2 nM). The phytoplankton response over the southern tropical IO is dominated by
629 increase in diatoms, which contribute to more than 60% of total phytoplankton biomass (Fig. 6). In contrast, over
630 the regions experiencing <1% chlorophyll increase, there is a shift from diatoms towards small phytoplankton
631 species (Fig. 6). For example, there is more than 80% reduction in diatoms and 50% increase in small
632 phytoplankton over the western AS. Other current systems such as the poleward flowing Somali current, the
633 eastward flowing Southwest Monsoon Current and its southward extension along the west coast of Indonesia also
634 transport sedimentary DFe to the open ocean, but such advection supports only ~5% phytoplankton biomass.

635 It is important to mention here that DFe bias arising from source strength has low impact on phytoplankton
636 response to a particular source of DFe. This is because the strongest phytoplankton response to a specific DFe
637 source is over the western AS and subtropical southern IO. As noted in Section 3.1, these regions have the least
638 magnitude of DFe bias. For example, averaging over the upper 100 m over the northern IO, atmospheric source
639 contributes ~13% to total chlorophyll concentration. Even after masking out the region to the east of 65°E
640 longitude over the AS, where the highest positive DFe bias arising from atmospheric Fe has been noted, it is seen
641 that atmospheric source contributes ~13% to the upper 100 m chlorophyll concentration. Similarly, sedimentary
642 sources contribute ~9% to the upper 100 m chlorophyll concentration over the entire northern IO domain. Masking
643 out BoB, where DFe bias is due to enhanced sediment transport, results in sedimentary source contributing ~8%
644 to the upper ocean chlorophyll concentration.

645

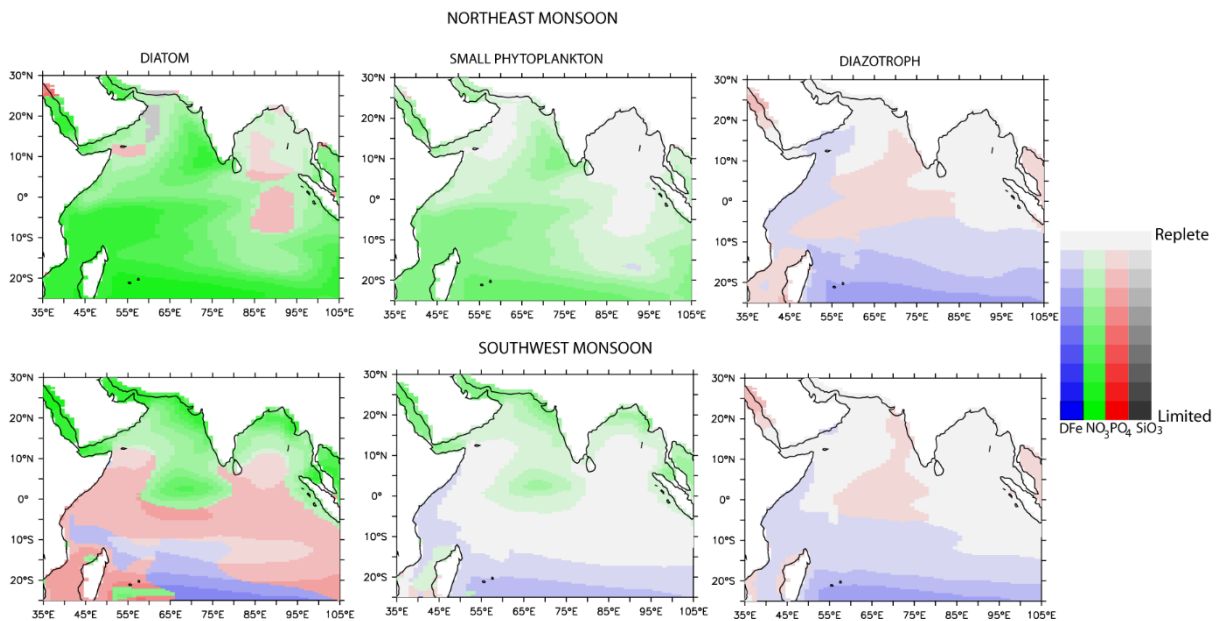
646 3.3.3 Role of background nutrients in phytoplankton responses to external iron

647

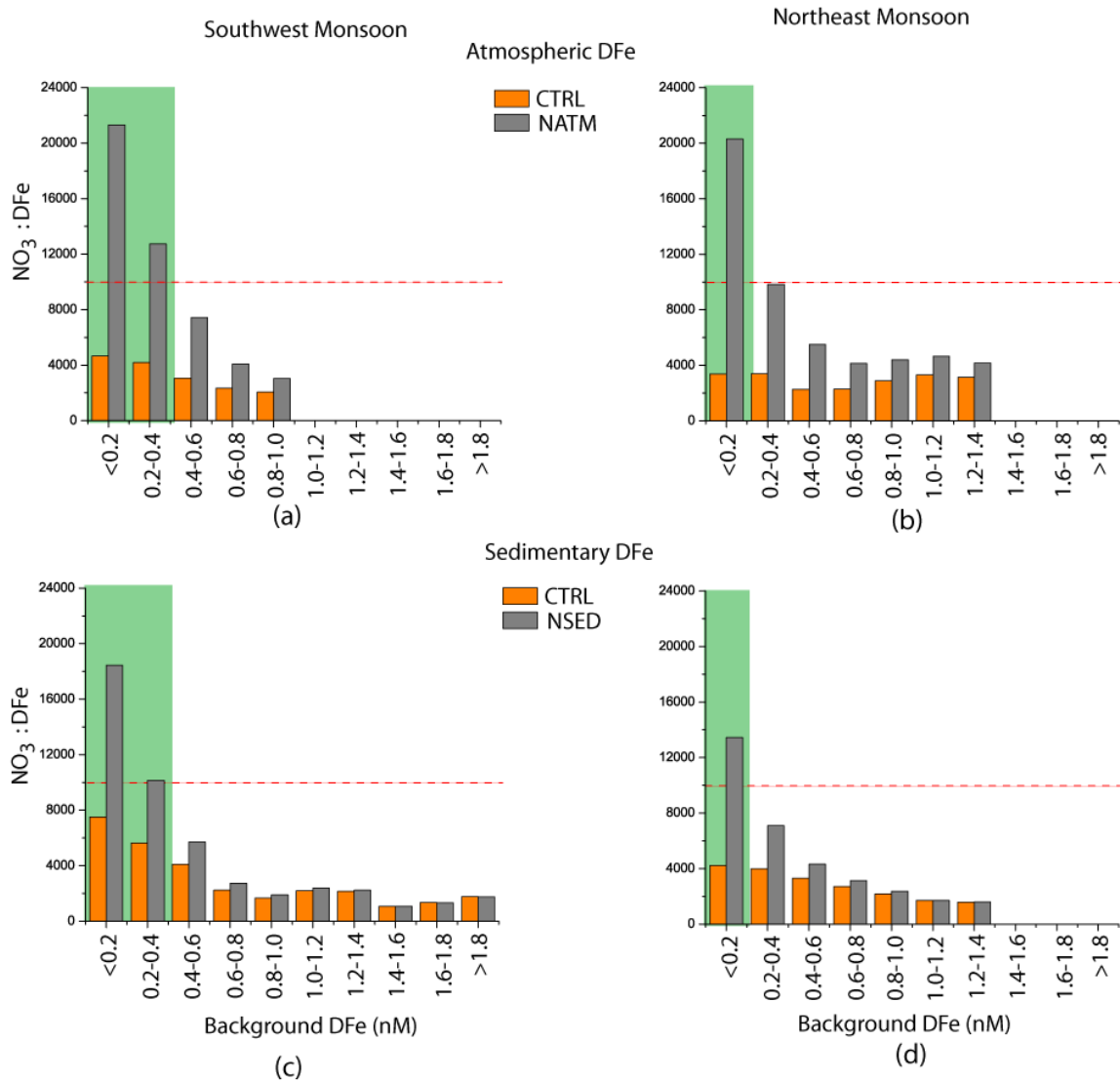
648 It emerges from the previous sections that there is heterogeneity in the phytoplankton response to atmospheric
649 and sedimentary sources of DFe. The regions of highest DFe input from a specific source are not always the
650 regions where strongest phytoplankton responses are evoked. What explains these differing patterns of
651 phytoplankton response? To examine this, patterns of nutrient limitations and iron supply from an external source
652 with respect to background DFe and nitrate (NO₃) concentrations are examined. In considering the phytoplankton
653 response to atmospheric sources (ATM case), background DFe is taken from the simulation without any
654 atmospheric source (NATM). Since river and hydrothermal sources make negligible contributions to DFe over
655 this domain, high levels of DFe in NATM mainly arise in regions where sedimentary sources are important.
656 Similarly, for estimating phytoplankton response to sedimentary sources (SED case), background DFe is taken
657 from simulation without any sedimentary source (NSED).

658 Generally, those regions experiencing greater than 1% increase in chlorophyll in response to atmospheric
659 (sedimentary) sources coincide with background DFe concentration <0.2-0.3 nM and high background NO₃:DFe
660 ratio from the NATM (NSED) simulation. For example, in NATM simulation, iron serves as the dominant nutrient
661 that limits productivity over the entire northern IO, with diatoms experiencing stronger iron limitation compared
662 to other phytoplankton groups (Fig. S10). Iron limitation is particularly severe over central and southern AS,
663 equatorial IO and the southern tropical IO. In NSED case, there is a switch from nitrate limitation to the north of
664 the intertropical convergence zone to iron limitation to the south of the intertropical convergence zone (Fig. S11).
665 While iron stress is alleviated with addition of external DFe, there is a shift towards macronutrient, especially

666 nitrate, limitation (Fig. 7). South of $\sim 15^{\circ}\text{S}$ latitude continues to experience iron limitation during June-September
 667 due to very low dust deposition. In contrast, regions where chlorophyll increase is $<1\%$ following DFe addition
 668 are characterized by nitrate limitation in NATM/NSED simulations and external DFe cannot alleviate this primary
 669 nutrient limitation. This is further illustrated in Fig. 8 where upper ocean $\text{NO}_3:\text{DFe}$ ratio is plotted against
 670 background DFe concentrations. Positive chlorophyll response is elicited in regions of lowest background DFe
 671 and highest background $\text{NO}_3:\text{DFe}$ ratio. Over the world oceans, a wide range of cellular $\text{DFe}:\text{C}$ ratios has been
 672 observed for diatoms, ranging from $100\ \mu\text{mol mol}^{-1}$ for DFe-replete conditions (Twining et al., 2015; 2021) to 2
 673 $\mu\text{mol mol}^{-1}$ for DFe-deplete conditions (de Baar et al., 2008). Assuming a C:N ratio of 117:16 (Anderson and
 674 Sarmiento, 1994), the range of N:DFe ratios obtained are ~ 1000 and ~ 68000 , respectively, for DFe-replete and
 675 DFe-deplete conditions. Similarly, by considering iron limitation taking place for $\text{DFe}:\text{C}$ ratio of $10\ \mu\text{mol mol}^{-1}$
 676 for open ocean species based on laboratory experiments (Sunda & Huntsman, 1995) and C:N ratio of 106:16,
 677 Measures and Vink (1999) have estimated that iron limitation over the AS water takes place at $\text{NO}_3:\text{DFe}$ ratio
 678 greater than ~ 15000 . In CESM simulations $>1\%$ increase in chlorophyll takes place when initial upper ocean $\text{NO}_3:$
 679 DFe ratio is more than 10,000 corresponding to Fe-limitation scenario (Fig. 8). With the addition of DFe from
 680 atmospheric or sedimentary sources, the upper ocean $\text{NO}_3:\text{DFe}$ ratio reduces to less than 4000 in some cases,
 681 thereby leading to N-limitation. Previously, iron addition experiments in AS during the southwest monsoon have
 682 shown that the positive chlorophyll response depends on initial nitrate concentrations, with this response
 683 increasing in magnitude with higher initial nitrate concentrations (Moffett et al., 2015). In summary, the initial
 684 upper ocean $\text{NO}_3:\text{DFe}$ ratio sets the ultimate limit to the magnitude and distribution of phytoplankton response
 685 following external DFe additions.
 686



687
 688
 689 **Figure 7: Patterns of surface nutrient limitations for different phytoplankton functional types from CTRL simulation.**
 690 **Green: nitrate; blue: iron; red: phosphate; grey: silicate limitations.**
 691



692

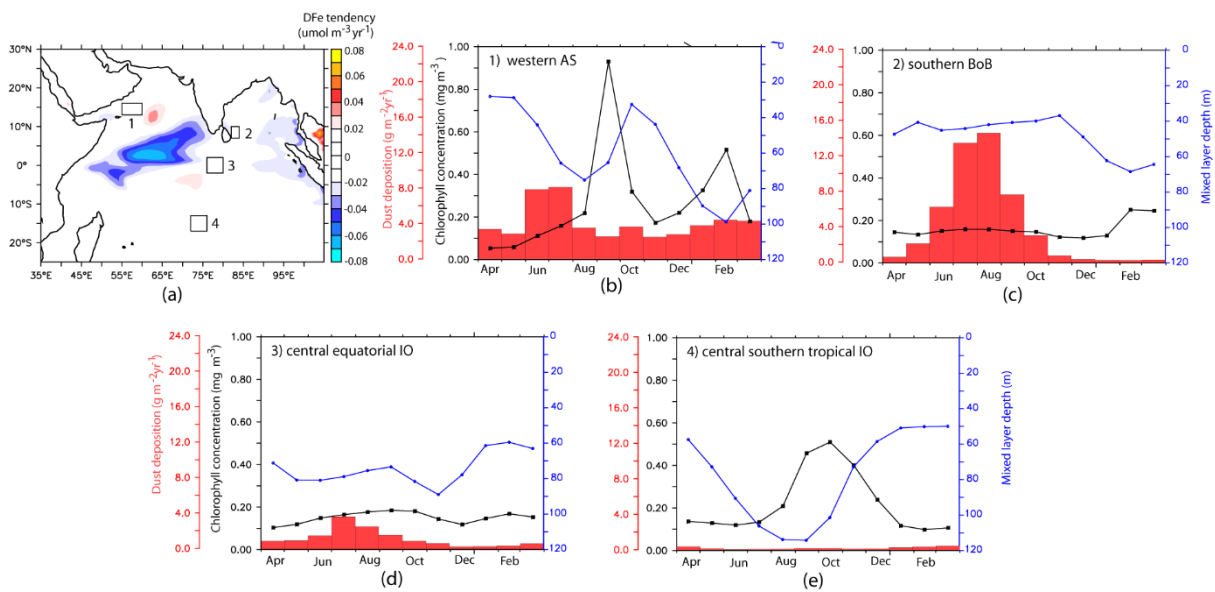
693 **Figure 8:** Relation between background nutrients and phytoplankton response for atmospheric (a and b) and
 694 sedimentary (c and d) sources of DFe during (a and c) southwest monsoon and (b and d) northeast monsoon. The
 695 horizontal axis shows background DFe concentrations. The orange columns show upper ocean $\text{NO}_3 : \text{DFe}$ ratio for
 696 CTRL case and grey columns show $\text{NO}_3 : \text{DFe}$ ratio for (a-b) NATM and (c-d) NSED cases. The red dashed lines show
 697 the location where $\text{NO}_3 : \text{DFe}$ ratio is 10,000: below this value N-limitation prevails in CESM. Green shades highlight
 698 the regions where >1% increase in chlorophyll following DFe addition from a specific source is induced.
 699

700 To sum up, atmospheric deposition is the most important source of DFe to the upper 100 m over the entire northern
 701 IO, followed by sedimentary sources. While atmospheric DFe is deposited over wide areas of the open ocean,
 702 sedimentary DFe fluxes arise only from continental shelves and are transported to open oceans through advection
 703 by currents. River and hydrothermal sources make negligible contributions to the total iron budget in the upper
 704 100 m. The primary response to atmospheric DFe is an increase in column-integrated phytoplankton biomass over
 705 most of the northern IO. In contrast, sedimentary source of iron is responsible for increases in column-integrated
 706 phytoplankton biomass mainly to the south of the intertropical convergence zone, where dust depositions are low.
 707 In general, significant positive responses of phytoplankton to addition of DFe are simulated only where low levels
 708 of background DFe concentrations and high values of background $\text{NO}_3 : \text{DFe}$ ratio are present. Otherwise, nitrate
 709 becomes the limiting nutrient once DFe is added. The simulations also show that positive chlorophyll response

710 to addition of DFe generally involves proliferation of diatoms, except over the equatorial IO where small
 711 phytoplankton increase is seen.

712
 713 **3.4 Iron budgets across different bio-physical regimes**

714 This section explores the main processes controlling DFe budget with respect to the role of atmospheric and
 715 sedimentary sources over different bio-physical regimes of the northern IO: (1) the western AS, (2) the southern
 716 BoB, (3) the central equatorial IO and (4) the central southern tropical IO. These regions encompass a wide range
 717 of productivity, with the first region being highly productive with OC-CCI chlorophyll exceeding 1.5 mg m^{-3} . The
 718 southern BoB and central southern tropical IO are moderately productive. Lastly, the central equatorial IO is
 719 oligotrophic with surface chlorophyll concentration being $\sim 0.1 \text{ mg m}^{-3}$. The locations of these regions along with
 720 CESM simulated seasonal cycles of mixed layer depths, chlorophyll and dust depositions are shown in Fig. 9.



721
 722 **Figure 9:** (a) Net DFe tendency averaged over the upper 100 m for the study period. The boxes indicate the regions
 723 chosen for further studying DFe budget in Section 3.4. (b-e) Seasonal cycle of dust deposition (red columns), mixed
 724 layer depth (blue curves) and chlorophyll concentrations (black curves) from CESM-CTRL case for the four regions
 725 marked in (a).

726
 727 The net dissolved iron tendency ($TEND_{DFe}$) is calculated as:

$$TEND_{DFe} = EXT + ADV + MIX + BIO \quad (3)$$

728
 729 where the source terms on the right describe dust/sediments/rivers/vents (EXT), horizontal and vertical advection
 730 (ADV), horizontal and vertical mixing (MIX) and biological sources/sinks (BIO). Advection includes explicitly
 731 resolved velocity as well as an additional “bolus” velocity from parameterization of mesoscale eddies (Gent &
 732 McWilliams, 1990). Vertical mixing includes a tracer gradient dependent term for cross-isopycnal mixing and a
 733 non-local mixing term, which accounts for mixing due to convective and shear instabilities (Large et al., 1994).
 734 Lateral mixing involves parameterization of mesoscale eddy-induced horizontal diffusion along isopycnal
 735 surfaces (Redi, 1982). The BIO term includes DFe losses due to biological iron uptake and scavenging, recycling

736 of iron back to the pool via remineralization, and iron released from phytoplankton and zooplankton losses and
737 grazing.

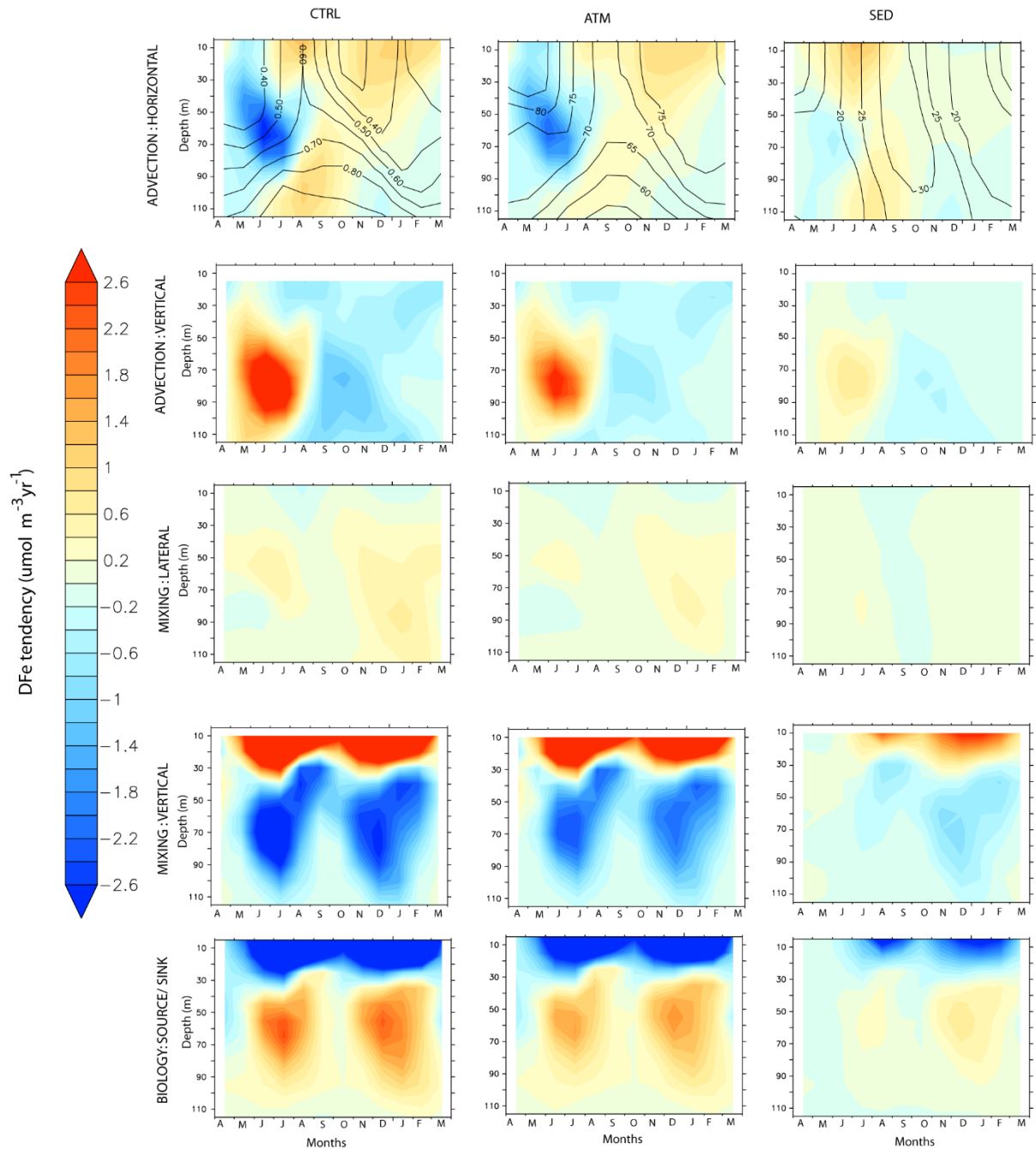
738 3.4.1 Western Arabian Sea

739 The western AS, off Oman and Yemen coastlines (considered here as 13°-16°N and 55°-60°E), is the most
740 productive region in the northern IO. Primary productivity in the western AS is highest during southwest monsoon
741 (Fig. 9b), during which alongshore southwesterly winds lead to upwelling and bring subsurface nutrients from
742 depths of ~150-200 m (Morrison et al., 1998). Some of this upwelled water advects eastwards, transporting
743 nutrients that enhance productivity in the central AS (Prasanna Kumar et al., 2001). The region also experiences
744 a secondary bloom during northeast monsoon due to winter convection that deepens the mixed layer. Integrated
745 over depths of the euphotic zone, average primary productivity over the western AS during mid and late southwest
746 monsoon is estimated at $135 \pm 10 \text{ mmol C m}^{-2} \text{ d}^{-1}$ and $110 \pm 11 \text{ mmol C m}^{-2} \text{ d}^{-1}$ respectively (Barber et al., 2001). In
747 comparison, primary productivity over the western AS during mid and late northeast monsoon is $137 \pm 13 \text{ mmol}$
748 $\text{C m}^{-2} \text{ d}^{-1}$ and $88 \pm 4 \text{ mmol C m}^{-2} \text{ d}^{-1}$ (Barber et al., 2001). Although this region encounters high dust deposition
749 (Haake et al., 1993; Mahowald et al., 2009), *in situ* measurements have hypothesized possible iron limitation
750 during late southwest monsoon because upwelled water is drawn from above the iron-rich sub-oxic zone (Naqvi
751 et al., 2010).

752 The largest peak in dust deposition is during southwest monsoon, followed by a second peak during northeast
753 monsoon (Fig. 9b). Accordingly, the upper ocean DFe concentration is highest during southwest monsoon and is
754 dominated by atmospheric sources (Fig. 10). Sedimentary contribution, although much lower, peaks during late
755 southwest monsoon and fall intermonsoon months. Throughout the year DFe concentration increases with depth,
756 thus pointing to consumption by phytoplankton at the surface. Vertical advection and vertical mixing are the most
757 important physical mechanisms governing DFe supply within this region during southwest monsoon (Fig. 10).
758 These processes begin to strengthen from May onwards to reach their peak during June-July and decrease
759 thereafter. Decomposing DFe advection tendency into tendencies arising from gradients in tracer distribution
760 (DFe') and velocity convergence (U') respectively, it is seen that vertical advection of DFe arises from DFe' and
761 U' in equal magnitude. However, the former process is dominant in June and the latter process dominates during
762 July (Fig. S12). The maximum vertical advection of DFe is centered around 80 m depth and progressively reduces
763 at shallower depths, as the vertical velocity reduces towards the surface. Vertical mixing prevailing in the upper
764 40 m brings this vertically advected DFe from subsurface to the surface. Furthermore, horizontal advection plays
765 an important role in redistributing this DFe supplied by vertical processes, with contributions from horizontal U'
766 being at least twice as large as DFe' . During spring and early southwest monsoon, northeastward horizontal
767 advection removes atmospheric deposited DFe throughout the upper 100 m, while aiding the supply of
768 sedimentary DFe from Somalia and Omani continental shelves to the western AS. Later in the year as the
769 southwest monsoon current circulation is established, and meridional currents along the western AS become
770 stronger, its effect is first evident in the south along the Somali coast and progresses northward with time. The
771 result is convergence of both atmospheric and sedimentary DFe in the western AS during July-September. During
772 northeast monsoon, vertical mixing driven by winter convection, with the mixed layer deepening to 100 m, is the
773 most important means of DFe supply, from both atmospheric and sedimentary sources, into the surface layer.

774 Additionally, horizontal advection by westward currents transports DFe from atmospheric deposition in the central
775 AS into the western AS.

776 Removal of DFe from the water column is mainly through biological uptake in the upper 40 m. Uptake of DFe by
777 small phytoplankton dominate biological uptake throughout the year, except during September-October when
778 diatoms uptake of DFe becomes significant (not shown). This signature of diatoms is also observed in opal fluxes
779 measured by sedimentary traps deployed near the western AS and has been attributed to lowering of zooplankton
780 grazing pressures during late southwest monsoon (Smith, 2001) as well as to silicate limitation of diatoms in
781 initially upwelled waters (Haake et al., 1993). In the subsurface layer, remineralization of sinking fluxes of
782 particulate iron peaking at ~50 m replenishes the DFe pool during the latter part of the productive months (Fig.
783 S16a). Iron so released is made available to the surface layer via mixing or advection, thereby playing an important
784 role in maintaining surface DFe pool. Some of the remineralized DFe is further removed by scavenging, which
785 peaks at ~80 m during the productive months due to large fluxes of sinking particulate organic carbon, biogenic
786 silica, calcium carbonate and dust (Fig. S16a). Atmospheric deposition dominates biological source/sink of DFe
787 throughout the year, while sedimentary DFe is more important for biology during northeast monsoon months.



788
 789 **Figure 10:** Evolution of the various terms of DFe budget, expressed as $\mu\text{mol m}^{-3} \text{yr}^{-1}$, by month and depth over the
 790 western Arabian Sea. Left panels: CTRL, Middle panels: ATM and, Right panels: SED case. The contours in the upper
 791 panel for CTRL show evolution of DFe concentrations (nM), while the contours in the upper panels for ATM and SED
 792 cases show the percentage contribution of each of these cases to total DFe concentrations in CTRL case.

793

794 3.4.2 Southern Bay of Bengal

795 The region corresponding to the southern BoB (7° - 10° N and 82° - 84° E) is located to the east of Sri Lanka.
 796 Compared to the rest of the BoB, freshwater flux from South Asian rivers reduces markedly in this region due to
 797 advection of high salinity water from AS by the eastward flowing Southwest Monsoon Current (see Fig. 2h) as
 798 well as upward pumping of saltier water by thermocline doming during the southwest monsoon season
 799 (Vinayachandran et al., 2013). This leads to stronger biophysical coupling in the southern BoB, compared to the
 800 rest of the bay, through erosion of the upper stable layer of freshwater capping. During southwest monsoon, the

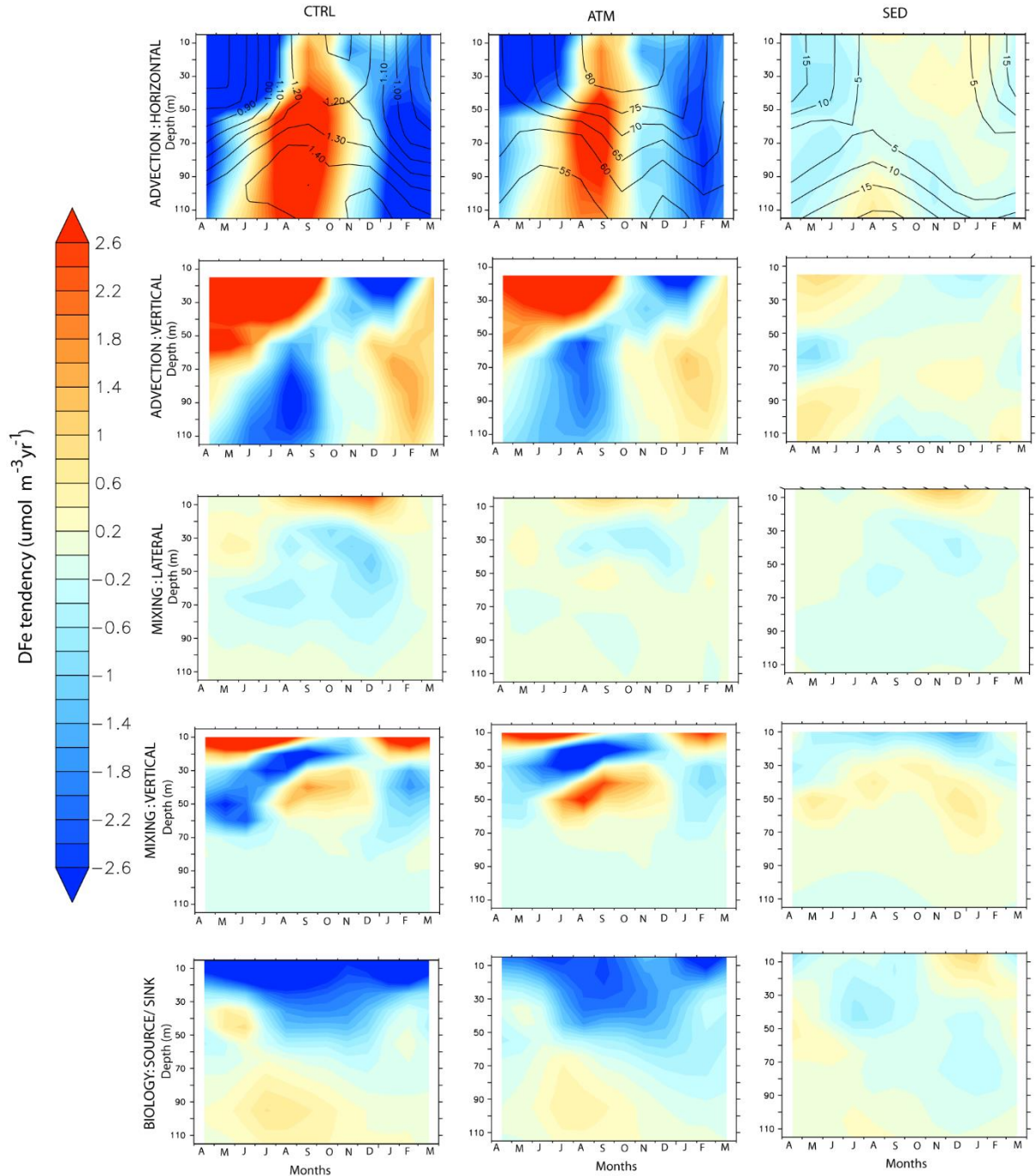
801 Southwest Monsoon Current advects nutrients and chlorophyll from the upwelling regions along the southern tip
802 of India and Sri Lanka into the southern BoB (Vinayachandran et al., 2004). Over the open southern BoB, to the
803 east of Sri Lanka, cyclonic wind stress curl drives open ocean upwelling leading to shoaling of the thermocline
804 that forms the Sri Lankan dome. This results in surface chlorophyll concentration between 0.3-0.7 mg m⁻³ and
805 strong subsurface chlorophyll maxima between 20-50 m where chlorophyll concentration can exceed 1 mg m⁻³
806 (Thushara et al., 2019). A much lower magnitude of surface chlorophyll concentration (~0.18 mg m⁻³, Fig. 9c)
807 and subsurface chlorophyll maxima (~0.2 mg m⁻³) at 40-60 m depth is simulated by CESM. During the northeast
808 monsoon, CESM simulates a second bloom over this region associated with winter cooling and mixed layer
809 deepening to ~60 m (Fig. 9c). This bloom has slightly higher magnitude, peaking at ~0.25 mg m⁻³, compared to
810 the southwest monsoon bloom. Surface chlorophyll data from OC-CCI also reveals the presence of northeast
811 monsoon blooms (peak at ~0.25 mg m⁻³), which during some years are of higher magnitude than southwest
812 monsoon blooms. Argo data in this region also show signatures of mixed layer deepening during winter (not
813 shown).

814 Overall, the highest DFe over this region is encountered during the late southwest monsoon and is dominated by
815 atmospheric deposition (Fig. 11). Vertical advection is the most important process supplying DFe to the surface
816 layers during spring and southwest monsoon months (Fig. 11). This is aided by a positive wind stress curl
817 established over the region from March onwards. While vertical velocity is positive during the southwest monsoon
818 over the entire depth considered, DFe supply by vertical advection is positive only for depths less than 50 m (Fig.
819 S13). This is because the magnitude of upward velocity gradually reduces with depth, resulting in positive values
820 of U' upwards from 40 m depths. (Fig. S13). With the arrival of westward propagating Rossby waves to the
821 western boundary of the BoB during October, upwelling favorable vertical motion collapses (Webber et al., 2018).

822 With respect to horizontal advection, it is seen that the magnitude and sign of convergence by the meridional
823 component of the current mainly controls DFe supply over the southern BoB. This arises from the southward
824 flowing current to the western flank of the Sri Lankan dome that supplies atmospheric DFe to this region. This
825 DFe supplied by the southwards current, as well as DFe derived from upwelling, is removed by the energetic
826 eastward currents during late spring to early fall intermonsoon months. During the rest of the year, the westward
827 flowing currents supplies some sedimentary DFe from the Andaman Sea to the southern BoB. However, the much
828 larger magnitude of dust deposition in the north-western BoB leads to overall negative tracer gradients and, thus,
829 dilution of DFe by horizontal advection. The most important DFe supply mechanism during northeast monsoon
830 is enhanced vertical mixing in the upper 20 m associated with deepening of mixed layer. Additionally,
831 downwelling due to weakly negative wind stress curl during this time of the year removes DFe from the surface
832 and favors its accumulation in the subsurface ocean. Lateral mixing complements DFe supply to the upper 20 m
833 during fall and early northeast monsoon, especially from sedimentary sources.

834 Biological uptake removes DFe throughout the year from the upper 40 m especially during the southwest and
835 northeast monsoon blooms (Fig. 11). DFe uptake in the upper 40 m is dominated by small phytoplankton during
836 most of the year, except during northeast monsoon (not shown). Diatom DFe uptake, on the other hand, dominates
837 the deep chlorophyll maxima present between 40-70 m throughout the year as well as within the surface layer
838 during northeast monsoon months. Several studies have pointed to substantial nutrient uptake by diatoms in the
839 central, coastal, and northern BoB due to riverine supply of silicates (Madhu et al., 2006; Madhupratap et al.,

840 2003). Remineralization of particulate iron as well as iron release from grazing and mortality of phytoplankton
 841 and zooplankton have a primary peak between 50 m-80 m during July-August and secondary peak during
 842 February-March. On the contrary, scavenging removes DFe, with its effect peaking during July-August during
 843 blooms (Fig. S16b).



844
 845 **Figure 11:** Same as Figure 10, except over the southern Bay of Bengal.

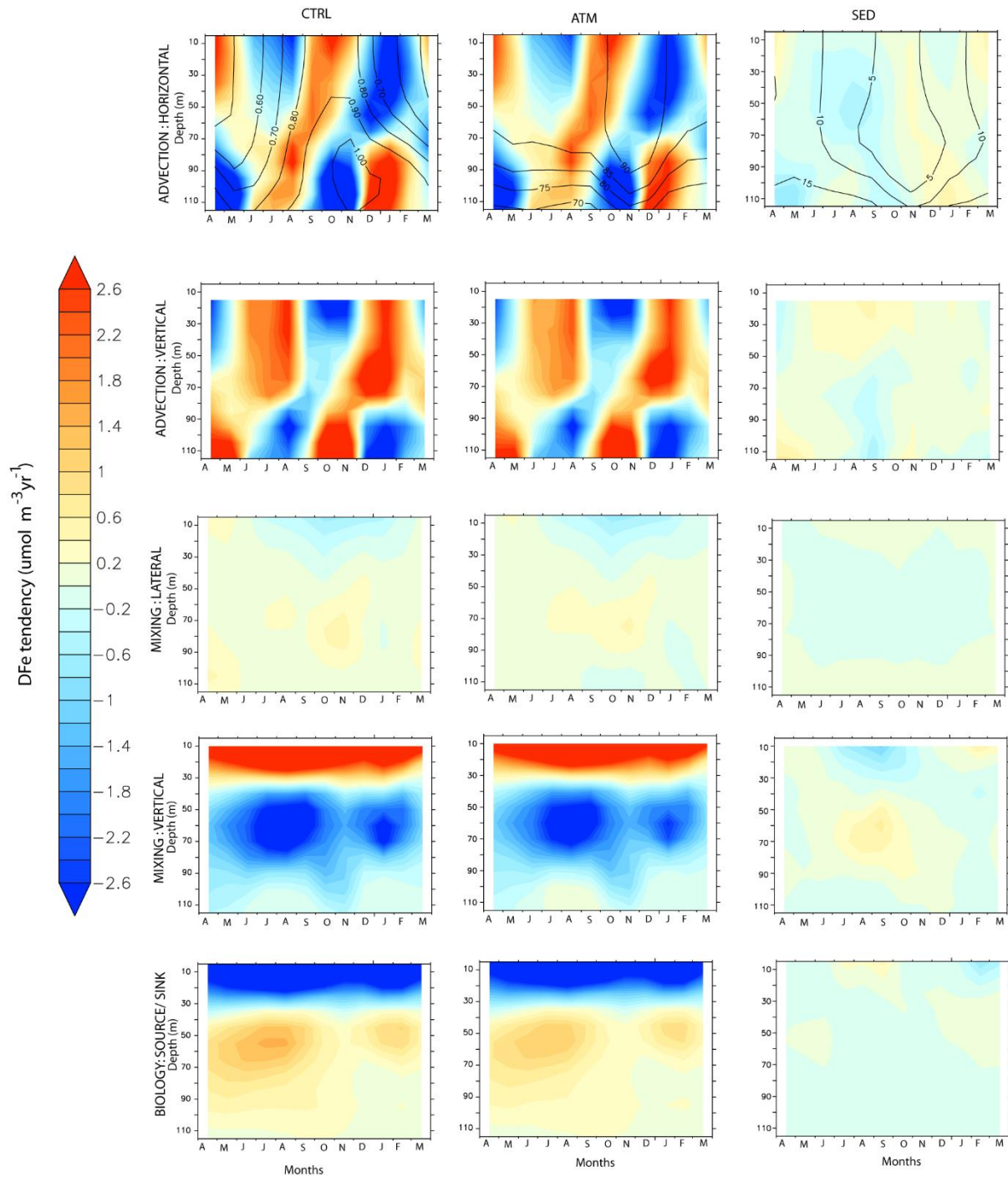
846
 847 **3.4.3 Central Equatorial IO**

848 With chlorophyll concentrations around 0.1 mg m⁻³ for most part of the year, the central equatorial IO (2°S-2°N
 849 and 76°-80°E) is the least productive of all the regions considered (Fig. 9d). Unlike its counterparts in the Pacific

850 and the Atlantic Oceans, the equatorial IO experiences only transient upwelling due to changes in wind direction
851 associated with migration of the intertropical convergence zone. This also leads to surface currents reversing their
852 direction four times a year. Thus, the region experiences westward surface currents of weak magnitude during the
853 southwest and northeast monsoon months and much stronger eastwards current during the spring and fall
854 intermonsoon months (Han et al., 1999). These narrow eastwards surface currents during the intermonsoon
855 months, known as Wyrтки jets, are in response to westerly winds (Wyrтки, 1973). The biogeochemical
856 characteristics of the region have only been recently explored with the help of satellite and *in situ* data (e.g.,
857 Prasanna Kumar et al., 2012; Strutton et al., 2015). Deepening of the surface layer associated with the eastward
858 transport of water during the intermonsoon months lowers productivity (Prasanna Kumar et al., 2012).
859 Chlorophyll concentrations, although much lower compared to the rest of the IO, peaks during October-December
860 possibly due to wind stirring or shear instability at the base of the eastward moving Wyrтки Jet (Strutton et al.,
861 2015). Additionally, *in situ* measurements in the central equatorial IO have revealed deep chlorophyll maxima
862 located ~60 m depth contributing to more than 30% of the total chlorophyll biomass (Vidya et al., 2013). The
863 peak ocean DFe concentration is encountered during August-November. Overall, comparison between CTRL,
864 ATM and SED cases show that atmospheric deposition, peaking during July (Fig. 9d), dominates DFe contribution
865 to the central equatorial IO, whereas sedimentary DFe plays a distant secondary role (Fig. 12).

866 Horizontal advection is the most important process of DFe supply within the mixed layer during March-May and
867 September-November (Fig. 12). During the intervening months, vertical advection plays the predominant role in
868 DFe supply. Decomposing the horizontal advection further into $D\text{Fe}'$ and U' reveals that the meridional velocity
869 convergence is the main contributor to the central equatorial IO DFe budget during March-May and September-
870 November (Fig. S14). This originates from the westerly wind directing equatorward Ekman flow in both the
871 hemispheres, which leads to convergence and drives eastward propagating downwelling Kelvin wave (McPhaden
872 et al., 2015). Averaged over the upper 100 m, zonal velocity convergence, although somewhat of lower magnitude,
873 opposes meridional velocity convergence throughout the year. When the Wyrтки jet weakens, upwelling induced
874 by easterly wind drives upward vertical supply of DFe, whereas there is downward vertical removal of DFe during
875 the intervening periods. This alternating between upwelling and downwelling control on DFe has an upward phase
876 propagation. An important feature of the central equatorial IO, in contrast to other equatorial regions, is the
877 presence of transient Equatorial Undercurrent between 60 m-200 m depth with core generally centered on the
878 depth of the 20°C isotherm (Chen et al., 2015). The Equatorial Undercurrent appears most strongly during winter-
879 spring months and with much weaker magnitude during summer-fall months (Chen et al., 2015; Schott &
880 McCreary, 2001). CESM simulation reveals the signature of the upper part of the Equatorial Undercurrent in
881 influencing DFe budget. This is characterized by the zonal velocity underneath the mixed layer (~80 m depth)
882 showing strong eastward transport during January-April and a much weaker eastward transport during September-
883 November. The horizontal convergence of DFe is prominent during the developing phase of the Equatorial
884 Undercurrent (December-February and June-August), probably, associated with progressive eastward extension
885 and strengthening of Equatorial Undercurrent from the western IO. These periods of horizontal DFe convergence
886 are interspersed with vertical DFe convergence. Superimposed on advection, vertical mixing plays an important
887 role in bringing subsurface DFe to the surface levels in the upper 30 m, peaking during July-August.

888 Biological removal of DFe, almost entirely by small phytoplankton, is conspicuous in the upper 40 m and peaks
889 during September. This is in line with sediment trap studies over the central equatorial IO where peak biogenic
890 fluxes are detected during the southwest and fall intermonsoon months and are dominated by coccolithophorids
891 and foraminifera carbonate (Ramaswamy and Gaye, 2006). Furthermore, *in situ* water samples have shown that
892 picoplankton, having size less than 10 μm , consists of more than 90% of the phytoplankton biomass in central
893 equatorial IO (Vidya et al., 2013). The period of peak biogenic flux is also characterized by peak in DFe removal
894 by scavenging and remineralization of particulate iron released from mortality and grazing at deeper layers (Fig.
895 S16c). A secondary increase in biological removal of DFe is noticed during January-March associated with a
896 secondary peak in chlorophyll, although its impact is not evident in sediment trap biogenic flux data (Vidya et al.,
897 2013). This might arise from remineralization of particulate iron being almost twice the magnitude of scavenging
898 losses during this time of the year.



899

900 **Figure 12:** Same as Figure 10, except over the central equatorial Indian Ocean.

901

902 3.4.4 Central Southern Tropical IO

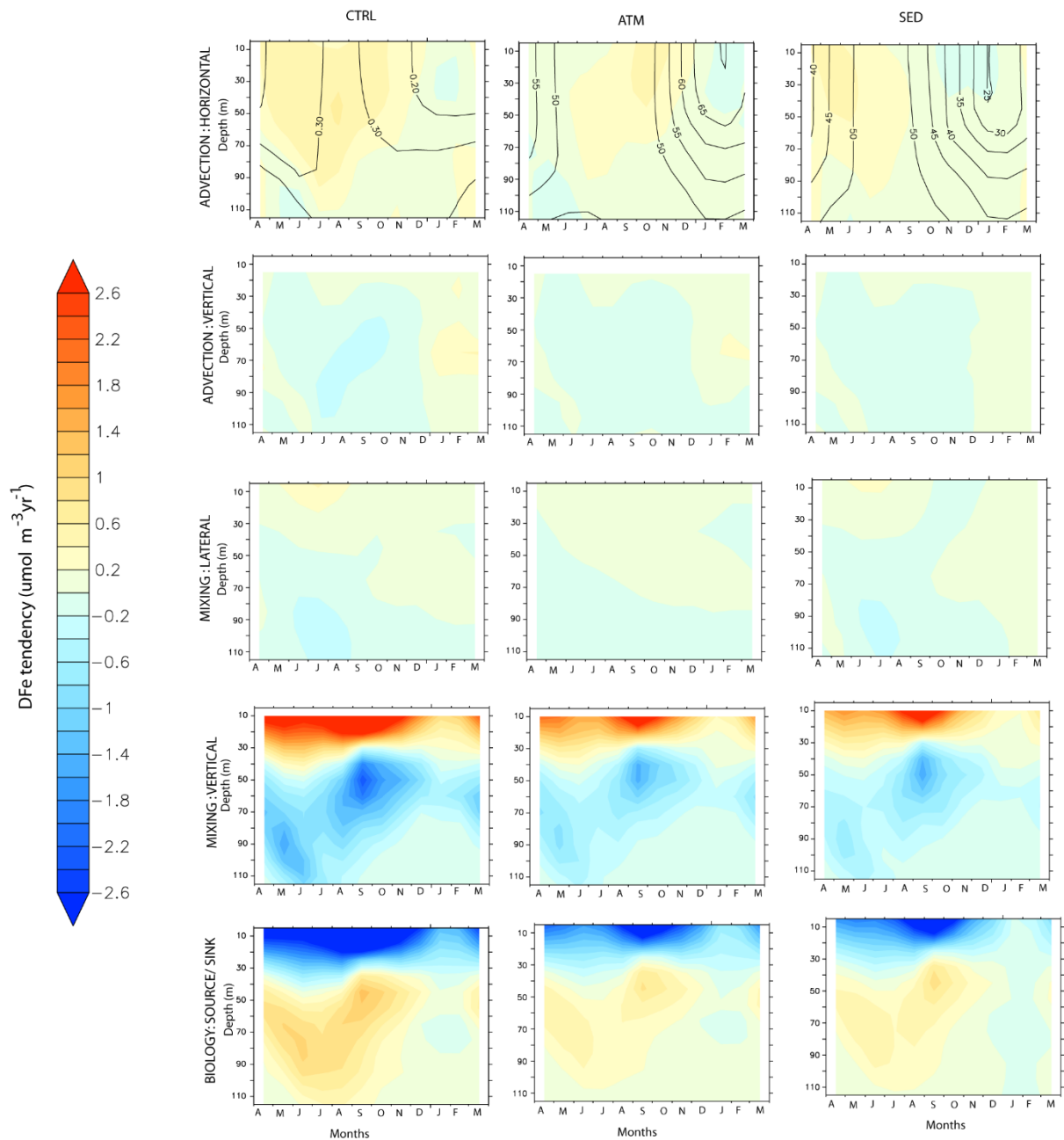
903 The central southern tropical IO (13°-17°S and 72°-76°E) is located in the transition zone between DFe-poor region
 904 of the subtropical IO gyre and DFe-enriched northern IO. Of all the regions considered, this receives the lowest
 905 atmospheric DFe (Fig. 9e), resulting in DFe limitation of phytoplankton growth particularly during the boreal
 906 summer (Fig. 7). Steady southeasterly winds, prevailing throughout the year, transport dust from Australian
 907 sources into this region. Peak in dust deposition is during austral spring and summer associated with strong source

908 activity (Kok et al., 2021; Yang et al., 2021). A secondary peak in dust deposition during austral winter is possibly
909 associated with enhanced transport. Northern part of the central southern tropical IO lies on the Seychelles-Chagos
910 thermocline ridge, which is characterized by doming up of the thermocline due to negative wind stress curl
911 resulting in Ekman divergence (Vialard et al., 2009). The thermocline progressively deepens towards the sub-
912 tropical southern IO gyre to the south as wind stress curl changes sign to positive. The westward flowing South
913 Equatorial Current brings low salinity water and nutrients from the Indonesian region. Satellite observed enhanced
914 chlorophyll concentration during the boreal (austral) summer (winter) months have been attributed to vertical
915 diffusion (Košić et al., 2009; Lévy et al., 2007). Additionally, westward propagating upwelling/downwelling
916 Rossby waves arrive in this region following La Nina/El Nino event and play a key role in modulating sea surface
917 height and the depth of thermocline (Masumoto & Meyers, 1998; Périgaud & Delecluse, 1992). This perturbs the
918 depth of nitracline, which has significant impact on column productivity (Kawamiya & Oschlies, 2001).

919 Both ATM and SED sources are important in this region for DFe supply, with the SED (ATM) source having
920 higher contribution during austral winter (summer) months (Fig. 13). Analysis of CESM-simulated DFe budget
921 reveals that vertical mixing in the upper 30 m is the most important process of DFe supply, which peaks during
922 September. This is the time of the year when CESM records the lowest sea surface temperature resulting in mixed
923 layer deepening. Such winter mixing leads to erosion of vertical gradient in DFe observed during the rest of the
924 year in the upper 120 m. Horizontal advection is the next most important supplier of DFe in this region. The
925 westward flowing South Equatorial Current is strongest during austral winter and during winter-to-summer
926 transition months. This results in meridional velocity convergence and zonal velocity divergence resulting in a
927 quasi-balance between DFe supply and removal (Fig. S15). Overall, horizontal advection leads to predominantly
928 sedimentary DFe convergence during March-June and predominantly atmospheric DFe convergence during
929 September-November.

930 The wind stress curl is mostly negative, that is upwelling favorable, throughout the year. Between April-October
931 (austral winter), when winter convection-driven blooms are prominent, wind stress curl becomes weakly negative
932 to slightly positive. Following this, during January-March, the wind stress curl becomes strongly negative
933 resulting in upward velocity and favors vertical advection of both atmospheric and sedimentary DFe in equal
934 magnitude. While vertical U' is responsible for supplying DFe in the upper 50 m, vertical DFe' is important at
935 deeper depths (Fig. S15).

936 The biological sink of DFe peaks during the month of maximum vertical mixing, that is, during September.
937 During this time, uptake of DFe is dominated by diatoms, which accounts for more than 80% of the total DFe
938 uptake. Small phytoplankton dominate the rest of the year. Scavenging removal of DFe and particulate iron
939 remineralization peaks one month later during October between 50-90 m depth range (Fig. S16d). Overall, the
940 central southern tropical IO is the only region where atmospheric deposition and sedimentary sources of iron are
941 equally important in driving the DFe budget.



942

943 **Figure 13:** Same as **Figure 10**, except over the central southern tropical Indian Ocean.

944

945 **4 Conclusions**

946

947 Using the ocean component of the Earth system model CESM version 2.1, this study elucidates the impacts of
 948 various sources of DFe on upper ocean productivity, nutrient limitations and DFe budgets over the northern IO.
 949 The iron cycle in CESM represents the complex interplay between several processes including DFe supply,
 950 removal by scavenging and biological uptake, particulate iron remineralization, and organic ligand complexation.
 951 The major sources of DFe for this region are included in this model: atmospheric deposition, sediments,
 952 hydrothermal vents, and rivers. Although there are model biases in representing physical and biogeochemical
 953 variables, the overall patterns of spatial and temporal variation of DFe are simulated reasonably well in CESM.

954 The study finds that atmospheric deposition is the most important source of DFe to the northern IO. Atmospheric
955 deposition contributes well over 50% of the total DFe concentration and more than 10% (35%) to upper 100 m
956 (surface level) chlorophyll concentrations, especially over the AS, equatorial IO, and southern tropical IO.
957 Sedimentary sources become important along continental shelves, where they can contribute to more than 20% of
958 total DFe. The sedimentary source has the largest impact in fueling phytoplankton blooms over the southern
959 tropical IO during June-September. In contrast, hydrothermal and river sources have negligible impacts on upper
960 ocean DFe pools in this region. Almost all regions that experience significant positive chlorophyll responses to
961 atmospheric as well as sedimentary sources of DFe show a preponderance of diatoms over other phytoplankton
962 groups. The increases in phytoplankton following external DFe addition are evoked in regions with low
963 background DFe levels (<0.3 nM) and high initial NO₃:DFe, indicating the importance of high levels of
964 macronutrients. Following, external DFe addition, a shift to nitrate limitation of phytoplankton is observed.

965 Analysis of DFe budget across different biophysical regimes in the northern IO shows that this budget is generally
966 dominated by atmospheric deposition, with sedimentary sources of DFe being a distant second contributor. The
967 exception to this occurs over the southern tropical IO region, where both atmospheric and sedimentary sources
968 become equally important. In all the regions considered, vertical mixing is the most important physical mechanism
969 through which DFe is supplied, and furthermore this mechanism is active almost throughout the year. In contrast,
970 the importance of horizontal and vertical advection is highly seasonal. DFe uptake by small phytoplankton in the
971 upper ocean is the most important route through which DFe removal takes place, except in the productive waters
972 where diatoms also participate in the removal process. At subsurface levels, competition between the removal of
973 DFe by scavenging and remineralization of particulate iron determines the DFe pool available to the surface ocean
974 via these aforementioned physical processes.

975 Of all DFe sources, atmospheric deposition is most likely vulnerable to future global warming, and changes to it
976 will perhaps exert strong influence on upper ocean productivity and nutrient limitation. Additionally, 59% of the
977 continental shelves and bathyal sea floor over the northern IO experiences hypoxic conditions (Helly and Levin,
978 2004) and there are several lines of evidence pointing to reductions in oxygen content over this region during the
979 last few decades due to enhanced upper ocean stratification (Schmidtko et al., 2017). This will possibly impact
980 the flux of iron from reduced sediments. The present study thus provides foundations to explore how different
981 future scenarios of atmospheric deposition and the extent of reducing sediments can impact biogeochemistry over
982 the northern IO.

983

984 **Code and data availability**

985 Climatology of ocean temperature, salinity and nutrients are from World Ocean Atlas 2018 available at
986 <https://www.ncei.noaa.gov/access/world-ocean-atlas-2018/> . Monthly surface chlorophyll data from OC-CCI is
987 obtained from <https://www.oceancolour.org/>. Monthly climatology of ocean mixed layer depth based on Holte at
988 al. (2017) is downloaded from <http://mixedlayer.ucsd.edu/>. Surface ocean current data from OSCAR can be
989 downloaded from: [https://podaac.jpl.nasa.gov/dataset/OSCAR_L4_OC_third-](https://podaac.jpl.nasa.gov/dataset/OSCAR_L4_OC_third-deg?ids=Keywords:Keywords:Projects&values=Oceans::Solid%20Earth::OSCAR&provider=PODAAC)
990 [deg?ids=Keywords:Keywords:Projects&values=Oceans::Solid%20Earth::OSCAR&provider=PODAAC](https://podaac.jpl.nasa.gov/dataset/OSCAR_L4_OC_third-deg?ids=Keywords:Keywords:Projects&values=Oceans::Solid%20Earth::OSCAR&provider=PODAAC).

991 Dissolved iron from GEOTRACES Intermediate Data Product 2021 is available at
992 <https://www.geotraces.org/geotraces-intermediate-data-product-2021/>. Additionally, dissolved iron profile data

993 are also obtained from Tagliabue et al. (2012) available at <https://www.bodc.ac.uk/geotraces/data/historical/>. The
994 code for CESM2.1 can be downloaded from https://www.cesm.ucar.edu/models/cesm2/release_download.html
995 (last access: 01 December 2020).

996 **Author contributions**

997 PB conceived the study, carried out model simulations, analysed the data and wrote the manuscript.

998 **Competing interests**

999 The author declares that there is no conflict of interest.

1000 **Acknowledgments**

1001 PB acknowledges the computational facilities provided by Supercomputer Education and Research Centre
1002 (SERC) at the Indian Institute of Science for carrying out CESM simulations.

1003 **Financial support**

1004 The author is supported by Department of Science and Technology INSPIRE Faculty scheme
1005 (DST/INSPIRE/04/2018/002625).

1006 **References**

1007 [Anand, S. S., Rengarajan, R., Sarma, V. V. S. S., Sudheer, A. K., Bhushan, R., and Singh, S. K.: Spatial variability](#)
1008 [of upper ocean POC export in the Bay of Bengal and the Indian Ocean determined using particle-reactive \$^{234}\text{Th}\$,
1009 \[J. Geophys. Res.-Oceans, 122, 3753–3770, <https://doi.org/10.1002/2016JC012639>, 2017.\]\(#\)](#)

1010 [Anand, S. S., Rengarajan, R., Shenoy, D., Gauns, M., and Naqvi, S. W. A.: POC export fluxes in the Arabian Sea](#)
1011 [and the Bay of Bengal: A simultaneous \$^{234}\text{Th}\$ / \$^{238}\text{U}\$ and \$^{210}\text{Po}\$ / \$^{210}\text{Pb}\$ study, Mar. Chem., 198, 70–87,
1012 \[<https://doi.org/10.1016/j.marchem.2017.11.005>, 2018.\]\(#\)](#)

1013 Anderson, L. and Sarmiento, J.: Redfield ratios of remineralization determined by nutrient data analysis, Global
1014 Biogeochem. Cy., 8, 65–80, <https://doi.org/10.1029/93GB03318>, 1994.

1015 Armstrong, R. A., Lee, C., Hedges, J. I., Honjo, S., and Wakeham, S.: A new, mechanistic model for organic
1016 carbon fluxes in the ocean: based on the quantitative association of POC with ballast minerals, Deep-Sea Res.,
1017 49, 219–236, 2002.

1018 Banerjee, P. and Kumar, S. P.: Dust-induced episodic phytoplankton blooms in the Arabian Sea during winter
1019 monsoon, J. Geophys. Res.-Oceans, 119, 7123–7138,
1020 <https://doi.org/10.1002/2014JC010304>, 2014.

1021 Banerjee, P., Satheesh, S. K., Moorthy, K. K., Nanjundiah, R. S., and Nair, V. S.: Long-range transport of mineral
1022 dust to the northeast Indian Ocean: Regional versus remote sources and the implications, J. Clim., 32, 1525–1549,
1023 <https://doi.org/10.1175/JCLI-D-18-0403.1>, 2019.

1024 Barber, R. T., Marra, J., Bidigare, R. C., Codispoti, L. A., Halpern, D., Johnson, Z., Latasa, M., Goericke, R., and
1025 Smith, S. L.: Primary productivity and its regulation in the Arabian Sea during 1995, *Deep-Sea. Res. Pt. II*, 48,
1026 1127–1172, [https://doi.org/10.1016/S0967-0645\(00\)00134-X](https://doi.org/10.1016/S0967-0645(00)00134-X), 2001.

1027 Beal, L. M., Ffield, A., and Gordon, A. L.: Spreading of Red Sea overflow waters in the Indian Ocean, *J. Geophys.*
1028 *Res.*, 105, 8549–8564, <https://doi.org/10.1029/1999JC900306>, 2000.

1029 Bianchi, D., Dunne, J. P., Sarmiento, J. L., and Galbraith, E. D.: Data-based estimates of suboxia, denitrification,
1030 and N₂O production in the ocean and their sensitivities to dissolved O₂, *Global Biogeochem. Cy.*, 26, GB2009,
1031 <https://doi.org/10.1029/2011gb004209>, 2012.

1032 Blain, S., Quéguiner, B., Armand, L., Belviso, S., Bombled, B., Bopp, L., Bowie, A., Brunet, C., Brussaard, C.,
1033 Carlotti, F., Christaki, U., Corbière, A., Durand, I., Ebersbach, F., Fuda, J.-L., Garcia, N., Gerringa, L., Griffiths,
1034 B., Guigue, C., Guillermin, C., Jacquet, S., Jeandel, C., Laan, P., Lefèvre, D., Lo Monaco, C., Malits, A., Mosseri,
1035 J., Obernosterer, I., Park, Y.-H., Picheral, M., Pondaven, P., Remenyi, T., Sandroni, V., Sarthou, G., Savoye, N.,
1036 Scouarnec, L., Souhaut, M., Thuiller, D., Timmermans, K., Trull, T., Uitz, J., van Beek, P., Veldhuis, M., Vincent,
1037 D., Viollier, E., Vong, L., and Wagener, T.: Effect of natural iron fertilization on carbon sequestration in the
1038 Southern Ocean, *Nature*, 446, 1070–1074, <https://doi.org/10.1038/nature05700>, 2007.

1039 Boss, E. and Behrenfeld, M.: In situ evaluation of the initiation of the North Atlantic phytoplankton bloom,
1040 *Geophys. Res. Lett.*, 37, L18603, <https://doi.org/10.1029/2010GL044174>, 2010.

1041 ~~Boyd, P. W., Jickells, T., Law, C. S., Blain, S., Boyle, E. A., Buesseler, K. O., Coale, K. H., Cullen, J. J., de Baar,~~
1042 ~~H. J. W., Follows, M., Harvey, M., Lancelot, C., Levasseur, M., Owens, N. P. J., Pollard, R., Rivkin, R. B.,~~
1043 ~~Sarmiento, J., Schoemann, V., Smetacek, V., Takeda, S., Tsuda, A., Turner, S., and Watson, A. J.: Mesoscale Iron~~
1044 ~~Enrichment Experiments 1993–2005: Synthesis and Future Directions, *Science*, 315, 612–617,~~
1045 ~~<https://doi.org/10.1126/science.1131669>, 2007.~~

1046 Boyd, P. W. and Ellwood, M. J.: The biogeochemical cycle of iron in the ocean, *Nat. Geosci.*, 3, 675–682,
1047 <https://doi.org/10.1038/ngeo964>, 2010.

1048 Buck, K. N., Lohan, M. C., Berger, C. J., and Bruland, K. W.: Dissolved iron speciation in two distinct river
1049 plumes and an estuary: Implications for riverine iron supply, *Limnol. Oceanogr.*, 52, 843–855,
1050 <https://doi.org/10.4319/lo.2007.52.2.0843>, 2007.

1051 ~~[Buesseler, K., Ball, L., Andrews, J., Benitez-Nelson, C., Belostock, R., Chai, F., and Chao, Y.: Upper ocean export](https://doi.org/10.1016/S0967-0645(98)80022-2)~~
1052 ~~[of particulate organic carbon in the Arabian Sea derived from thorium-234, *Deep-Sea Res. Pt. II*, 45, 2461–2487,](https://doi.org/10.1016/S0967-0645(98)80022-2)~~
1053 ~~[https://doi.org/10.1016/S0967-0645\(98\)80022-2](https://doi.org/10.1016/S0967-0645(98)80022-2), 1998.~~

1054 Canfield, D. E.: The geochemistry of river particulates from the continental USA: Major elements, *Geochim.*
1055 *Cosmochim. Ac.*, 61, 3349–3365, [https://doi.org/10.1016/s0016-7037\(97\)00172-5](https://doi.org/10.1016/s0016-7037(97)00172-5), 1997.

1056 Chen, G., Han, W., Li, Y., Wang, D., and McPhaden, M. J.: Seasonal-to-interannual time-scale dynamics of the
1057 equatorial undercurrent in the Indian Ocean, *J. Phys. Oceanogr.*, 45, 1532–1553, [https://doi.org/10.1175/JPO-D-](https://doi.org/10.1175/JPO-D-14-0225.1)
1058 [14-0225.1](https://doi.org/10.1175/JPO-D-14-0225.1), 2015.

1059 Chinni, V., Singh, S. K., Bhushan, R., Rengarajan, R., and Sarma, V. V. S. S.: Spatial variability in dissolved iron
1060 concentrations in the marginal and open waters of the Indian Ocean, *Marine Chem.*, 208, 11–28,
1061 <https://doi.org/10.1016/j.marchem.2018.11.007>, 2019.

1062 Chinni, V., and Singh, S. K.: Dissolved iron cycling in the Arabian Sea and sub-tropical gyre region of the Indian
1063 Ocean, *Geochim. Cosmochim. Ac.*, 317, 325–348, <https://doi.org/10.1016/j.gca.2021.10.026>, 2022.

1064 ~~Coale, K. H., Johnson, K. S., Fitzwater, S. E., Gordon, R. M., Tanner, S., Chavez, F. P., Ferioli, L., Sakamoto, C.,
1065 Rogers, P., Millero, F., Steinberg, P., Nightingale, P., Cooper, D., Cochlan, W. P., Landry, M. R., Constantinou,
1066 J., Rollwagen, G., Trasvina, A., and Kudela, R.: A massive phytoplankton bloom induced by an ecosystem scale
1067 iron fertilization experiment in the equatorial Pacific Ocean, *Nature*, 383, 495–501,
1068 <https://doi.org/10.1038/383495a0>, 1996.~~

1069 Conway, T. M. and John, S. G.: Quantification of dissolved iron sources to the North Atlantic Ocean, *Nature*, 511,
1070 212–215, <https://doi.org/10.1038/nature13482>, 2014.

1071 Dai, A., Qian, T., Trenberth, K. E., and Milliman, J. D.: Changes in continental freshwater discharge from 1948
1072 to 2004, *J. Climate*, 22, 2773–2792, <https://doi.org/10.1175/2008JCLI2592.1>, 2009.

1073 Danabasoglu, G., Bates, S. C., Briegleb, B. P., Jayne, S. R., Jochum, M., Large, W. G., Peacock, S., and Yeager,
1074 S. G.: The CCSM4 ocean component, *J. Climate*, 25, 1361–1389, <https://doi.org/10.1175/JCLI-D-11-00091.1>,
1075 2012.

1076 Danabasoglu, G., Lamarque, J.-F., Bacmeister, J., Bailey, D. A., DuVivier, A. K., Edwards, J., Emmons, L. K.,
1077 Fasullo, J., Garcia, R., Gettelman, A., Hannay, C., Holland, M. M., Large, W. G., Lauritzen, P. H., Lawrence, D.
1078 M., Lenaerts, J. T. M., Lindsay, K., Lipscomb, W. H., Mills, M. J., Neale, R., Oleson, K. W., Otto-Bliesner, B.,
1079 Phillips, A. S., Sacks, W., Tilmes, S., van Kampenhout, L., Vertenstein, M., Bertini, A., Dennis, J., Deser, C.,
1080 Fischer, C., Fox-Kemper, B., Kay, J. E., Kinnison, D., Kushner, P. J., Larson, V. E., Long, M. C., Mickelson, S.,
1081 Moore, J. K., Nienhouse, E., Polvani, L., Rasch, P. J., and Strand, W. G., The Community Earth System Model
1082 Version 2 (CESM2), *J. Adv. Model. Earth Syst.*, 12, e2019MS001916, <https://doi.org/10.1029/2019MS001916>,
1083 2020.

1084 de Baar, H. J. W., Boyd, P. W., Coale, K. H., Landry, M. R., Tsuda, A., Assmy, P., Bakker, D. C. E., Bozec, Y.,
1085 Barber, R. T., Brzezinski, M. A., Buesseler, K. O., Boye, M., Croot, P. L., Gervais, F., Gorbunov, M. Y., Harrison,
1086 P. J., Hiscock, W. T., Laan, P., Lancelot, C., Law, C. S., Levasseur, M., Marchetti, A., Millero, F. J., Nishioka, J.,
1087 Nojiri, Y., van Oijen, T., Riebesell, U., Rijkenberg, M. J. A., Saito, H., Takeda, S., Timmermans, K. R., Veldhuis,
1088 M. J. W., Waite, A. M., and Wong, C.-S.: Synthesis of iron fertilization experiments: From the Iron Age in the
1089 Age of Enlightenment, *J. Geophys. Res.*, 110, C09S16, <https://doi.org/10.1029/2004JC002601>, 2005.

1090 de Baar, H., Gerringa, L., Laan, P., and Timmermans, K.: Efficiency of carbon removal per added iron in ocean
1091 iron fertilization, *Mar. Ecol. Prog. Ser.*, 364, 269–282, <https://doi.org/10.3354/meps07548>, 2008.

1092 Dohan, K. and Maximenko, N.: Monitoring ocean currents with satellite sensors, *Oceanography*, 23, 94–103,
1093 2010.

- 1094 Dutkiewicz, S., Ward, B. A., Monteiro, F., and Follows, M. J.: Interconnection between nitrogen fixers and iron
1095 in the Pacific Ocean: Theory and numerical model, *Global Biogeochem. Cy.*, 26, GB1012,
1096 <https://doi.org/10.1029/2011GB004039>, 2012.
- 1097 Elrod, V. A., Berelson, W. M., Coale, K. H., and Johnson, K. S.: The flux of iron from continental shelf sediments:
1098 A missing source for global budgets, *Geophys. Res. Lett.*, 31, L12307, <https://doi.org/10.1029/2004GL020216>,
1099 2004.
- 1100 ~~Flegal, A.R., Smith, G.J., Gill, G.A., Sañudo-Wilhelmy, S., and Anderson, L.C.D.: Dissolved trace element cycles
1101 in the San Francisco Bay estuary, *Marine Chem.*, 36, 329–363, 1991.~~
- 1102 Gamo, T., Okamura, K., Hatanaka, H., Hasumoto, H., Komatsu, D., Chinen, M., Mori, M., Tanaka, J., Hirota, A.
1103 and Tsunogai, U.: Hydrothermal plumes in the Gulf of Aden, as characterized by light transmission, Mn, Fe, CH₄
1104 and delta C-13-CH₄ anomalies, *Deep-Sea Res. Pt. II*, 121, 62–70, 2015.
- 1105 Garcia, H. E., Locarnini, R. A., Boyer, T. P., Antonov, J. I., Baranova, O. K., Zweng, M. M., Reagan, J. R., and
1106 Johnson, D. R.: World Ocean Atlas 2013, Volume 3: Dissolved Oxygen, Apparent Oxygen Utilization, and
1107 Oxygen Saturation, edited by: Levitus, S. and Mishonov, A., NOAA Atlas NESDIS, 75, 27 pp., 2014a.
- 1108 Garcia, H. E., Locarnini, R. A., Boyer, T. P., Antonov, J. I., Baranova, O. K., Zweng, M. M., Reagan, J. R., and
1109 Johnson, D. R.: World Ocean Atlas 2013, Volume 4: Dissolved Inorganic Nutrients (phosphate, nitrate, silicate),
1110 edited by: Levitus, S. and Mishonov, A., NOAA Atlas NESDIS, 76, 25 pp., 2014b.
- 1111 Garcia H. E., Boyer, T. P., Baranova, O. K., Locarnini, R. A., Mishonov, A. V., Grodsky, A., Paver, C. R.,
1112 Weathers, K. W., Smolyar, I. V., Reagan, J. R., Seidov, D., Zweng, M. M.: World Ocean Atlas 2018: Product
1113 Documentation, edited by: Mishonov, A., 2019.
- 1114 Geider, R. J. and La Roche, J.: The role of iron in phytoplankton photosynthesis, and the potential for iron-
1115 limitation of primary productivity in the sea, *Photosynth. Res.*, 39, 275–301, <https://doi.org/10.1007/bf00014588>,
1116 1994.
- 1117 Gent, P. R. and McWilliams, J. C.: Isopycnal mixing in ocean circulation models, *J. Phys. Oceanogr.*, 20, 150–
1118 155, [https://doi.org/10.1175/1520-0485\(1990\)020<0150:IMIOCM>2.0.CO;2](https://doi.org/10.1175/1520-0485(1990)020<0150:IMIOCM>2.0.CO;2), 1990.
- 1119 Grand, M. M., Measures, C. I., Hatta, M., Hiscock, W. T., Buck, C. S., and Landing, W. M.: Dust deposition in
1120 the eastern Indian Ocean: The ocean perspective from Antarctica to the Bay of Bengal, *Global Biogeochem.*
1121 *Cycles*, 29, 357–374, <https://doi.org/10.1002/2014gb004898>, 2015.
- 1122 Guieu, C., Al Azhar, M., Aumont, O., Mahowald, N., Lévy, M., Éthé, C., and Lachkar, Z.: Major impact of dust
1123 deposition on the productivity of the Arabian Sea, *Geophys. Res. Lett.*, 46, 6736–6744, 2019
- 1124 Gustafsson, O., Kruså, M., Zencak, Z., Sheesley, R. J., Granat, L., Engström, E., Praveen, P. S., Rao, P. S., Leck,
1125 C., and Rodhe, H.: Brown clouds over South Asia: biomass or fossil fuel combustion?, *Science*, 323, 495–498,
1126 <https://doi.org/10.1126/science.1164857>, 2009.

- 1127 Haake, B., Ittekkot, V., Rixen, T., Ramaswamy, V., Nair, R. R., and Curry, W. B.: Seasonality and interannual
1128 variability of particle fluxes to the deep Arabian Sea, *Deep-Sea Res. Pt. I*, 40, 1323–1344, 1993.
- 1129 Han, W., McCreary, J. P., Anderson, D. L. T., and Mariano, A. J.: Dynamics of the eastern surface jets in the
1130 equatorial Indian Ocean, *J. Phys. Oceanogr.*, 29, 2191–2209, [https://doi.org/10.1175/1520-
1131 0485\(1999\)029<2191:DOTESJ>2.0.CO;2](https://doi.org/10.1175/1520-0485(1999)029<2191:DOTESJ>2.0.CO;2), 1999.
- 1132 [Harrison, C. S., Long, M. C., Lovenduski, N. S., and Moore, J. K.: Mesoscale Effects on Carbon Export: A Global
1133 Perspective. *Global Biogeochem. Cy.*, 32, 680–703, <https://doi.org/10.1002/2017GB005751>, 2018.](#)
- 1134 [Helly, J. J. and Levin, L. A.: Global distribution of naturally occurring marine hypoxia on continental margins,
1135 *Deep-Sea Res. Pt. I*, 51, 1159–1168, 2004.](#)
- 1136 Holte, J., Talley, L. D., Gilson, J., and Roemmich, D.: An Argo mixed layer climatology and database, *Geophys.
1137 Res. Lett.*, 44, 5618–5626, <https://doi.org/10.1002/2017GL073426>, 2017.
- 1138 Huffman, G. J., Adler, R. F., Arkin, P., Chang, A., Ferraro, R., Gruber, A., Janowiak, J., McNab, A., Rudolf, B.,
1139 and Schneider, U.: The Global Precipitation Climatology Project (GPCP) Combined Precipitation Dataset, *B. Am.
1140 Meteorol. Soc.*, 78, 5–20, [https://doi.org/10.1175/1520-0477\(1997\)078<0005:TGPCPG>2.0.CO;2](https://doi.org/10.1175/1520-0477(1997)078<0005:TGPCPG>2.0.CO;2), 1997.
- 1141 Ilyina, T., Six, K. D., Segschneider, J., Maier-Reimer, E., Li, H., and Núñez-Riboni, I.: Global ocean
1142 biogeochemistry model HAMOCC: Model architecture and performance as component of the MPI-Earth system
1143 model in different CMIP5 experimental realizations, *J. Adv. Model. Earth Sy.*, 5, 287–315,
1144 <https://doi.org/10.1029/2012MS000178>, 2013.
- 1145 Jickells, T. D., An, Z. S., Andersen, K. K., Baker, A. R., Bergametti, G., Brooks, N., Cao, J. J., Boyd, P. W., Duce,
1146 R. A., Hunter, K. A., Kawahata, H., Kubilay, N., laRoche, J., Liss, P. S., Mahowald, N., Prospero, J. M., Ridgwell,
1147 A. J., Tegen, I., and Torres, R.: Global Iron Connections between Desert Dust, Ocean Biogeochemistry, and
1148 Climate, *Science*, 308, 67–71, 2005.
- 1149 Jin, Q., Wei, J., Pu, B., Yang, Z. L., and Parajuli, S. P.: High summertime aerosol loadings over the Arabian Sea
1150 and their transport pathways, *J. Geophys. Res.-Atmos.*, 123, 10568–10590,
1151 <https://doi.org/10.1029/2018jd028588>, 2018.
- 1152 Johnson, K. S., Chavez, F. P., and Friederich, G. E.: Continental-shelf sediment as a primary source of iron for
1153 coastal phytoplankton, *Nature*, 398, 697–700, <https://doi.org/10.1038/19511>, 1999.
- 1154 Kalnay, E., Kanamitsu, M., Kistler, R., Collins, W., Deaven, D., Gandin, L., Iredell, M., Saha, S., White, G.,
1155 Woollen, J., Zhu, Y., Leetmaa, A., Reynolds, R., Chelliah, M., Ebisuzaki, W., Higgins, W., Janowiak, J., Mo, K.
1156 C., Ropelewski, C., Wang, J., Jenne, R., and Joseph, D.: The NCEP/NCAR 40-Year Reanalysis Project, *B. Am.
1157 Meteorol. Soc.*, 77, 437–471, [https://doi.org/10.1175/1520-0477\(1996\)077<0437:TNYRP>2.0.CO;2](https://doi.org/10.1175/1520-0477(1996)077<0437:TNYRP>2.0.CO;2), 1996.

- 1158 Kawamiya, M. and Oschlies, A.: Formation of a basin-scale surface chlorophyll pattern by Rossby waves,
1159 *Geophys. Res. Lett.*, 28, 4139–4142, 2001.
- 1160 Kohfeld, K. E. and Harrison, S. P.: DIRTMAP: the geological record of dust, *Earth-Science Rev.*, 54, 81–114,
1161 [https://doi.org/10.1016/S0012-8252\(01\)00042-3](https://doi.org/10.1016/S0012-8252(01)00042-3), 2001.
- 1162 Kok, J. F., Adebisi, A. A., Albani, S., Balkanski, Y., Checa-Garcia, R., Chin, M., Colarco, P. R., Hamilton, D. S.,
1163 Huang, Y., Ito, A., Klose, M., Li, L., Mahowald, N. M., Miller, R. L., Obiso, V., Pérez García-Pando, C., Rocha-
1164 Lima, A., and Wan, J. S.: Contribution of the world's main dust source regions to the global cycle of desert dust,
1165 *Atmos. Chem. Phys.*, 21, 8169–8193, <https://doi.org/10.5194/acp-21-8169-2021>, 2021.
- 1166 Koňe, V., Aumont, O., Lévy, M., and Resplandy, L.: Physical and Biogeochemical Controls of the Phytoplankton
1167 Seasonal Cycle in the Indian Ocean: A Modeling Study, *Geoph. Monog. Series*, 185, 147–166,
1168 <https://doi.org/10.1029/2008GM000700>, 2009.
- 1169 Kumar, A., Suresh, K., and Rahaman, W.: Geochemical Characterization of Modern Aeolian Dust over the
1170 Northeastern Arabian Sea: Implication for Dust Transport in the Arabian Sea, *Science of the Total Environment*,
1171 729, 138576, <https://doi.org/10.1016/j.scitotenv.2020.138576>, 2020.
- 1172 Kuttippurath, J., Sunanda, N., Martin, M. V., and Chakraborty, K.: Tropical storms trigger phytoplankton blooms
1173 in the deserts of north Indian Ocean, *NPJ Climate and Atmospheric Science*, 4, 11,
1174 <https://doi.org/10.1038/s41612-021-00166-x>, 2021.
- 1175 Large, W. G., McWilliams, J. C., and Doney, S. C.: Oceanic vertical mixing: A review and a model with a
1176 nonlocal boundary layer parameterization, *Rev. Geophys.*, 32, 363–403, 1994.
- 1177 Large, W. G. and Yeager, S. G.: The global climatology of an interannually varying air-sea flux data set, *Clim.*
1178 *Dynam.*, 33, 341–364, <https://doi.org/10.1007/s00382-008-0441-3>, 2009.
- 1179 Léon, J. F. and Legrand, M.: Mineral dust sources in the surroundings of the North Indian Ocean, *Geophys. Res.*
1180 *Lett.*, 30, 1309, <https://doi.org/10.1029/2002GL016690>, 2003.
- 1181 Letelier, R. M., Karl, D. M., Abbott, M. R., and Bidigare, R. R.: Light driven seasonal patterns of chlorophyll and
1182 nitrate in the lower euphotic zone of the North Pacific Subtropical Gyre, *Limnol. Oceanogr.*, 49, 508–519,
1183 <https://doi.org/10.4319/lo.2004.49.2.0508>, 2004.
- 1184 [Levitus, S., T. Boyer, M. Conrigh, D. Johnson, T. O'Brien, J. Antonov, C. Stephens, and R. Garfield:](#)
1185 [Introduction, Vol. I, World Ocean Database 1998, NOAA Atlas NESDIS 18, 346 pp, 1998.](#)
- 1186 Lévy, M., Shankar, D., André, J., Shenoi, S., Durand, F., and de Boyer Montégut, C.: Basin-wide seasonal
1187 evolution of the Indian Ocean's phytoplankton blooms, *J. Geophys. Res.-Oceans*, 112, C12014,
1188 <https://doi.org/10.1029/2007JC004090>, 2007.
- 1189 Liu, J. P., Xue, Z., Ross, K., Wang, H. J., Yang, Z. S., and Gao, S.: Fate of sediments delivered to the sea by Asian
1190 large rivers: Long-distance transport and formation of remote alongshore clinothems, *The Sedimentary Record*,
1191 7(4), 4–9, <https://doi.org/10.2110/sedred.2009.4.4>, 2009.

- 1192 Liu, X., Ma, P.-L., Wang, H., Tilmes, S., Singh, B., Easter, R. C., Ghan, S. J., and Rasch, P. J.: Description and
1193 evaluation of a new four-mode version of the Modal Aerosol Module (MAM4) within version 5.3 of the
1194 Community Atmosphere Model, *Geosci. Model Dev.*, 9, 505–522, <https://doi.org/10.5194/gmd-9-505-2016>,
1195 2016.
- 1196 Long, M. C., Moore, J. K., Lindsay, K., Levy, M. N., Doney, S. C., Luo, J. Y., Krumhardt, K. M., Letscher, R.
1197 T., Grover, M., and Sylvester, Z. T.: Simulations with the Marine Biogeochemistry Library (MARBL), *J. Adv.*
1198 *Model. Earth Syst.*, accepted, <https://doi.org/10.1029/2021MS002647>, 2021.
- 1199 Madhu, N., Jyothibabu, R., Maheswaran, P., Gerson, V. J., Gopalakrishnan, T., and Nair, K.: Lack of seasonality
1200 in phytoplankton standing stock (chlorophyll a) and production in the western Bay of Bengal, *Cont. Shelf Res.*,
1201 26, 1868–1883, 2006.
- 1202 Madhupratap, M., Prasanna Kumar, S., Bhattathiri, P. M. A., DileepKumar, M., Raghukumar, S., Nair, K. K. C.,
1203 and Ramaiah, N.: Mechanism of the biological response to winter cooling in the northeastern Arabian Sea, *Nature*,
1204 384, 549–552, 1996.
- 1205 Madhupratap, M., Gauns, M., Ramaiah, N., Kumar, S. P., Muraleedharan, P., de Sousa, S., Sardessai, S., and
1206 Muraleedharan, U.: Biogeochemistry of the Bay of Bengal: physical, chemical and primary productivity
1207 characteristics of the central and western Bay of Bengal during summer monsoon 2001, *Deep-Sea Res. Pt. II*, 50,
1208 881–896, [https://doi.org/10.1016/S0967-0645\(02\)00611-2](https://doi.org/10.1016/S0967-0645(02)00611-2), 2003.
- 1209 Mahowald, N. M., Engelstaedter, S., Luo, C., Sealy, A., Artaxo, P., Benitez-Nelson, C., Bonnet, S., Chen, Y.,
1210 Chuang, P. Y., Cohen, D. D., Dulac, F., Herut, B., Johansen, A. M., Kubilay, N., Losno, R., Maenhaut, W., Paytan,
1211 A., Prospero, J. M., Shank, L. M., and Siefert, R. L.: Atmospheric iron deposition: global distribution, variability,
1212 and human perturbations, *Ann. Rev. Mar. Sci.*, 1, 245–278,
1213 <https://doi.org/10.1146/annurev.marine.010908.163727>, 2009.
- 1214 Masumoto, Y. and Meyers, G.: Forced Rossby waves in the southern tropical Indian Ocean, *J. Geophys. Res.-*
1215 *Oceans*, 103, 27589–27602, <https://doi.org/10.1029/98JC02546>, 1998.
- 1216 Mayorga, E., Seitzinger, S. P., Harrison, J. A., Dumont, E., Beusen, A. H. W., Bouwman, A. F., Fekete, B. M.,
1217 Kroeze, C. and van Drecht, G.: Global Nutrient Export from WaterSheds 2 (NEWS 2): Model development and
1218 implementation, *Environ. Modell. Softw.*, 25, 837–853, <https://doi.org/10.1016/j.envsoft.2010.01.007>, 2010.
- 1219 McLennan, S. M.: Relationships between the trace element composition of sedimentary rocks and upper
1220 continental crust, *Geochemistry, Geophysics, Geosystems*, 2(4), 1021, <http://doi.org/10.1029/2000gc000109>,
1221 2001.
- 1222 McPhaden, M. J., Wang, Y., and Ravichandran, M.: Volume transports of the Wyrтки jets and their relationship
1223 to the Indian Ocean dipole, *J. Geophys. Res.-Oceans*, 120, 5302–5317, 2015.
- 1224 Measures, C. I. and Vink, S.: Seasonal variations in the distribution of Fe and Al in the surface waters of the
1225 Arabian Sea, *Deep-Sea Res. Pt. II*, 46, 1597–1622, 1999.

- 1226 Mills, M. M., Ridame, C., Davey, M., La Roche, J., and Geider, R. J.: Iron and phosphorus co-limit nitrogen
1227 fixation in the eastern tropical North Atlantic, *Nature*, 429, 292, <https://doi.org/10.1038/nature02550>, 2004.
- 1228 Moffett, J. W., Goepfert, T. J., and Naqvi, S. W. A.: Reduced iron associated with secondary nitrite maxima in
1229 the Arabian Sea, *Deep-Sea Res. Pt. I*, 54, 1341–1349, <https://doi.org/10.1016/j.dsr.2007.04.004>, 2007.
- 1230 Moffett, J. W., Vedamati, J., Goepfert, T. J., Pratihary, A., Gauns, M., and Naqvi, S. W. A.: Biogeochemistry of
1231 iron in the Arabian Sea, *Limnol. Oceanogr.*, 60, 1671–1688, <https://doi.org/10.1002/lno.10132>, 2015.
- 1232 Moore, J. K., Doney, S. C., and Lindsay, K.: Upper ocean ecosystem dynamics and iron cycling in a global three-
1233 dimensional model, *Global Biogeochem. Cy.*, 18, GB4028, <https://doi.org/10.1029/2004GB002220>, 2004.
- 1234 Moore, J. K. and Braucher, O.: Sedimentary and mineral dust sources of dissolved iron to the world ocean,
1235 *Biogeosciences*, 5, 631–656, <https://doi.org/10.5194/bg-5-631-2008>, 2008.
- 1236 Moore, C. M., Mills, M. M., Achterberg, E. P., Geider, R. J., La Roche, J., Lucas, M. I., McDonagh, E. I., Pan,
1237 X., Poulton, A. J., and Rijkenberg, M. J.: Large-scale distribution of Atlantic nitrogen fixation controlled by iron
1238 availability, *Nat. Geosci.*, 2, 867–871, 2009.
- 1239 Moore, C. M., Mills, M. M., Arrigo, K. R., Berman-Frank, I., Bopp, L., Boyd, P. W., Galbraith, E. D., Geider,
1240 R. J., Guieu, C., Jaccard, S. L., Jickells, T. D., Roche, J. L., Lenton, T. M., Mahowald, N. M., Marañón, E.,
1241 Marinov, I., Moore, J. K., Nakatsuka, T., Oschlies, A., Saito, M. A., Thingstad, T. F., Tsuda, A., and Ulloa, O.:
1242 Processes and patterns of oceanic nutrient limitation, *Nat. Geosci.*, 6, 701–710,
1243 <https://doi.org/10.1038/NGEO1765>, 2013a.
- 1244 Moore, J. K., Lindsay, K., Doney, S. C., Long, M. C., and Misumi, K.: Marine Ecosystem Dynamics and
1245 Biogeochemical Cycling in the Community Earth System Model CESM1(BGC): Comparison of the 1990s with
1246 the 2090s under the RCP4.5 and RCP8.5 Scenarios, *J. Climate*, 26, 9291–9312, <https://doi.org/10.1175/jcli-d-12-00566.1>, 2013b.
- 1248 Moorthy, K. K. and Babu, S. S.: Aerosol black carbon over Bay of Bengal observed from an island location, Port
1249 Blair: Temporal features and long-range transport, *J. Geophys. Res.*, 111, D17205, doi:10.1029/2005JD006855,
1250 2006.
- 1251 Morrison, J. M., Codispoti, L. A., Smith, S. L., Wishner, K., Flagg, C., Gardner, W. D., Gaurin, S., Naqvi, S.,
1252 Manghnani, V., Prosperie, L., and Gundersen, J. S.: The oxygen minimum zone in the Arabian Sea during 1995,
1253 *Deep-Sea Res. Pt. II*, 46, 1903–1931, 1999.
- 1254 Morrison, J. M., Codispoti, L. A., Gaurin, S., Jones, B., Manghanani, V., and Zheng, Z.: Seasonal variations of
1255 hydrographic and nutrient fields during the US JGOFS Arabian Sea Process Study, *Deep-Sea Res. Pt. II*, 45,
1256 2053–2101, 1998.

- 1257 Naqvi, S. W. A., Moffett, J. W., Gauns, M. U., Narvekar, P. V., Pratihary, A. K., Naik, H., Shenoy, D. M.,
 1258 Jayakumar, D. A., Goepfert, T. J., Patra, P. K., Al-Azri, A., and Ahmed, S. I.: The Arabian Sea as a high-nutrient,
 1259 low-chlorophyll region during the late Southwest Monsoon, *Biogeosciences*, 7, 2091–2100,
 1260 <https://doi.org/10.5194/bg-7-2091-2010>, 2010.
- 1261 Nishioka, J., Obata, H., and Tsumune, D.: Evidence of an extensive spread of hydrothermal dissolved iron in the
 1262 Indian Ocean, *Earth Planet. Sci. Lett.*, 361, 26–33, <https://doi.org/10.1016/j.epsl.2012.11.040>, 2013.
- 1263 Olsen, A., Key, R. M., van Heuven, S., Lauvset, S. K., Velo, A., Lin, X., Schirnick, C., Kozyr, A., Tanhua, T.,
 1264 Hoppema, M., Jutterström, S., Steinfeldt, R., Jeansson, E., Ishii, M., Pérez, F. F., and Suzuki, T.: The Global
 1265 Ocean Data Analysis Project version 2 (GLODAPv2) – an internally consistent data product for the world ocean,
 1266 *Earth Syst. Sci. Data*, 8, 297–323, <https://doi.org/10.5194/essd-8-297-2016>, 2016.
- 1267 Périgaud, C., and Delecluse, P.: Annual sea level variations in the southern tropical Indian Ocean from Geosat
 1268 and shallow water simulations, *J. Geophys. Res.*, 97, 20169–20178, <https://doi.org/10.1029/92JC01961>, 1992.
- 1269 Pham, A. L. D., and Ito, T.: Anthropogenic iron deposition alters the ecosystem and carbon balance of the Indian
 1270 Ocean over a centennial timescale, *J. Geophys. Res.-Oceans*, 126, e2020JC016475,
 1271 <https://doi.org/10.1029/2020JC016475>, 2021.
- 1272 Pollard, R. T., Salter, I., Sanders, R. J., Lucas, M. I., Moore, C. M., Mills, R. A., Statham, P. J., Allen, J. T., Baker,
 1273 A. R., Bakker, D. C. E., Charette, M. A., Fielding, S., Fones, G. R., French, M., Hickman, A. E., Holland, R. J.,
 1274 Hughes, J. A., Jickells, T. D., Lampitt, R. S., Morris, P. J., Nedelec, F. H., Nielsdottir, M., Planquette, H., Popova,
 1275 E. E., Poulton, A. J., Read, J. F., Seeyave, S., Smith, T., Stinchcombe, M., Taylor, S., Thomalla, S., Venables, H.
 1276 J., Williamson, R., and Zubkov, M. V.: Southern Ocean deep-water carbon export enhanced by natural iron
 1277 fertilization, *Nature*, 457, 577–580, <https://doi.org/10.1038/nature07716>, 2009.
- 1278 Prasanna Kumar, S., Madhupratap, M., Dileep Kumar, M., Muraleedharan, P. M., de Souza, S. N., Gauns, M.,
 1279 and Sarma, V. V. S. S.: High biological productivity in the central Arabian Sea during summer monsoon driven
 1280 by Ekman pumping and lateral advection, *Curr. Sci.*, 81, 1633–1638, 2001.
- 1281 Prasanna Kumar, S., Nuncio, M., Narvekar, J., Kumar, A., Sardesai, S., de Souza, S. N., Gauns, M., Ramaiah, N.,
 1282 and Madhupratap, M.: Are eddies nature's trigger to enhance biological productivity in the Bay of Bengal?,
 1283 *Geophys. Res. Lett.*, 31, L07309, <https://doi.org/10.1029/2003GL019274>, 2004.
- 1284 Prasanna Kumar, S., Divya David, T., Byju, P., Narvekar, J., Yoneyama, K., Nakatani, N., Ishida, A., Horii, T.,
 1285 Masumoto, Y., and Mizuno, K.: Bio-physical coupling and ocean dynamics in the central equatorial Indian Ocean
 1286 during 2006 Indian Ocean Dipole, *Geophys. Res. Lett.*, 39, L14601, [doi:10.1029/2012GL052609](https://doi.org/10.1029/2012GL052609), 2012.
- 1287 Ramaswamy, V. and Gaye, B.: Regional variations in the fluxes of foraminifera carbonate, coccolithophorid
 1288 carbonate and biogenic opal in the northern Indian Ocean, *Deep-Sea Res. Pt. I*, 53, 271–293,
 1289 [doi:10.1016/j.dsr.2005.11.003](https://doi.org/10.1016/j.dsr.2005.11.003), 2006.

- 1290 Ramaswamy, V., Gaye, B., Shirodkar, P. V., Rao, P. S., Chivas, A. R., Wheeler, D., and Thwin, S.: Distribution
1291 and sources of organic carbon, nitrogen and their isotopic signatures in sediments from the Ayeyarwady
1292 (Irrawaddy) continental shelf, northern Andaman Sea, *Marine Chem.*, 111(3), 137–150.
1293 <https://doi.org/10.1016/j.marchem.2008.04.006>, 2008.
- 1294 Raven, J. A.: The iron and molybdenum use efficiencies of plant growth with different energy, carbon and nitrogen
1295 sources, *New Phytol.*, 109, 279–287, <https://doi.org/10.1111/j.1469-8137.1988.tb04196.x>, 1988.
- 1296 Redi, M. H.: Oceanic isopycnal mixing by coordinate rotation, *J. Phys. Oceanogr.*, 12, 1154–1158,
1297 [https://doi.org/10.1175/1520-0485\(1982\)012<1154:OIMBCR>2.0.CO;2](https://doi.org/10.1175/1520-0485(1982)012<1154:OIMBCR>2.0.CO;2), 1982.
- 1298 Resplandy, L., Lévy, M., Madec, G., Pous, S., Aumont, O., and Kumar, D.: Contribution of mesoscale processes
1299 to nutrient budgets in the Arabian Sea, *J. Geophys. Res.*, 116, C11007, <https://doi.org/10.1029/2011JC007006>,
1300 2011.
- 1301 Rixen, T., Gaye, B., and Emeis, K.-C.: The monsoon, carbon fluxes, and the organic carbon pump in the northern
1302 Indian Ocean, *Prog. Oceanogr.*, 175, 24–39, <https://doi.org/10.1016/j.pocean.2019.03.001>, 2019.
- 1303 Robinson, R. A. J., Bird, M. I., Oo, N. W., Hoey, T. B., Aye, M. M., Higgitt, D. L., Lud, X. X., Swe, A., Tun, T.,
1304 and Win, S. L.: The Irrawaddy river sediment flux to the Indian Ocean: the original nineteenth-century data
1305 revisited, *J. Geol.*, 115, 629–640, <https://doi.org/10.1086/521607>, 2007.
- 1306 [Sander, S. and Koschinsky, A.:Metal flux from hydrothermal vents increased by organic complexation, *Nat.*](#)
1307 [*Geosci.*, 4, 145–150, <https://doi.org/10.1038/ngeo1088>, 2011.](#)
- 1308 Sathyendranath, S., Brewin, R. J., Brockmann, C., Brotas, V., Calton, B., Chuprin, A., Cipollini, P., Couto, A. B.,
1309 Dingle, J., Doerffer, R., Donlon, C., Dowell, M., Farman, A., Grant, M., Groom, S., Horseman, A., Jackson, T.,
1310 Krasemann, H., Lavender, S., Martinez-Vicente, V., Mazeran, C., Mélin, F., Moore, T. S., Müller, D., Regner, P.,
1311 Roy, S., Steele, C. J., Steinmetz, F., Swinton, J., Taberner, M., Thompson, A., Valente, A., Zühlke, M.,
1312 Brando, V. E., Feng, H., Feldman, G., Franz, B. A., Frouin, R., Gould, R. W., Hooker, S. B., Kahru, M.,
1313 Kratzer, S., Mitchell, B. G., Muller-Karger, F. E., Sosik, H. M., Voss, K. J., Werdell, J., and Platt, T.: An Ocean-
1314 Colour Time Series for Use in Climate Studies: The Experience of the Ocean-Colour Climate Change Initiative
1315 (OC-CCI), *Sensors*, 19, 4285, <https://doi.org/10.3390/s19194285>, 2019.
- 1316 Schlitzer, R., Masferrer Dodas, E., Adjou, M., Anderson, R. F., Andre, F., Cockwell, D. M., et al.: The
1317 GEOTRACES Intermediate Data Product 2021 (IDP2021), NERC EDS British Oceanographic Data Centre NOC,
1318 doi: 10.5285/cf2d9ba9-d51d-3b7c-e053-8486abc0f5fd, 2021.
- 1319 Schlosser, C., Klar, J. K., Wake, B. D., Snow, J. T., Honey, D. J., Woodward, E. M. S., Lohan, M. C., Achterberg,
1320 E. P., and Moore, C. M.: Seasonal ITCZ migration dynamically controls the location of the (sub)tropical Atlantic
1321 biogeochemical divide, *P. Natl. Acad. Sci. USA*, 111, 1438–1442, 2014.

- 1322 Schmidtko, S., Stramma, L., and Visbeck, M.: Decline in global oceanic oxygen content during the past five
1323 decades, *Nature*, 542, 335–339, <https://doi.org/10.1038/nature21399>, 2017.
- 1324 Schott, F. and McCreary, J. P.: The monsoon circulation of the Indian Ocean, *Prog. Oceanogr.*, 51, 1–123,
1325 [https://doi.org/10.1016/S0079-6611\(01\)00083-0](https://doi.org/10.1016/S0079-6611(01)00083-0), 2001.
- 1326 Sedwick, P. N. and DiTullio, G. R.: Regulation of algal blooms in Antarctic shelf waters by the release of iron
1327 from melting sea ice, *Geophys. Res. Lett.*, 24, 2515–2518, <https://doi.org/10.1029/97GL02596>, 1997.
- 1328 Singh, N. D., Chinni, V., and Singh, S. K.: Dissolved aluminium cycling in the northern, equatorial and subtropical
1329 gyre region of the Indian Ocean, *Geochim. Cosmochim. Ac.*, 268, 160–185, doi: 10.1016/j.gca.2019.09.028, 2020.
- 1330 ~~Sholkovitz, E. R.: The flocculation of dissolved Fe, Mn, Al, Cu, Ni, Co and Cd during estuarine mixing, *Earth*
1331 *Planet. Sc. Lett.*, 41, 77–86, [https://doi.org/10.1016/0012-821X\(78\)90043-2](https://doi.org/10.1016/0012-821X(78)90043-2), 1978.~~
- 1332 Sholkovitz, E. R., Sedwick, P. N., Church, T. M., Baker, A. R., and Powell, C. F.: Fractional solubility of aerosol
1333 iron: Synthesis of a global-scale data set, *Geochim. Cosmochim. Ac.*, 89, 173–189,
1334 <https://doi.org/10.1016/j.gca.2012.04.022>, 2012.
- 1335 Smith, R., Jones, P., Briegleb, B., Bryan, F., Danabasoglu, G., Dennis, J., Dukowicz, J., Eden, C., Fox-Kemper,
1336 B., Gent, P., Hecht, M., Jayne, S., Jochum, M., Large, W., Lindsay, K., Maltrud, M., Norton, N., Peacock, S.,
1337 Vertenstein, M., and Yeager, S.: The Parallel Ocean Program (POP) reference manual, Ocean component of the
1338 Community Climate System Model (CCSM), LANL Tech. Report, LAUR-10-01853, 141 pp., 2010.
- 1339 Smith, S. L.: Understanding the Arabian Sea: Reflections on the 1994-1996 Arabian Sea Expedition, *Deep-Sea*
1340 *Res. Pt. II*, 48, 1385–1402, 2001.
- 1341 Srinivas, B., Sarin, M. M., and Kumar, A.: Impact of anthropogenic sources on aerosol iron solubility over the
1342 Bay of Bengal and the Arabian Sea, *Biogeochemistry*, 110, 257–268, [https://doi.org/10.1007/s10533-011-9680-](https://doi.org/10.1007/s10533-011-9680-1)
1343 1, 2012.
- 1344 Srinivas, B. and Sarin, M. M.: Atmospheric dry-deposition of mineral dust and anthropogenic trace metals to the
1345 Bay of Bengal, *J. Mar. Syst.*, 126, 56–68, <https://doi.org/10.1016/j.jmarsys.2012.11.004>, 2013.
- 1346 Strutton, P. G., Coles, V. J., Hood, R. R., Matear, R. J., McPhaden, M. J., and Phillips, H. E.: Biogeochemical
1347 variability in the central equatorial Indian Ocean during the monsoon transition, *Biogeosciences*, 12, 2367–2382,
1348 <https://doi.org/10.5194/bg-12-2367-2015>, 2015.
- 1349 Sunda, W. G. and Huntsman, S. A.: Iron uptake and growth limitation in oceanic and coastal phytoplankton, *Mar.*
1350 *Chem.*, 50, 189–206, [https://doi.org/10.1016/0304-4203\(95\)00035-P](https://doi.org/10.1016/0304-4203(95)00035-P), 1995.

- 1351 Tagliabue, A., Bopp, L., Dutay, J.-C., Bowie, A. R., Chever, F., Jean-Baptiste, P., Bucciarelli, E., Lannuzel, D.,
1352 Remenyi, T., Sarthou, G., Aumont, O., Gehlen, M., and Jeandel, C.: Hydrothermal contribution to the oceanic
1353 dissolved iron inventory, *Nat. Geosci.*, 3, 252–256, <https://doi.org/10.1038/ngeo818>, 2010.
- 1354 Tagliabue, A., Mtshali, T., Aumont, O., Bowie, A. R., Klunder, M. B., Roychoudhury, A. N., and Swart, S.: A
1355 global compilation of dissolved iron measurements: focus on distributions and processes in the Southern Ocean,
1356 *Biogeosciences*, 9, 2333–2349, <https://doi.org/10.5194/bg-9-2333-2012>, 2012.
- 1357 Tagliabue, A., Aumont, O., and Bopp, L.: The impact of different external sources of iron on the global carbon
1358 cycle, *Geophys. Res. Lett.*, 41, 920–926, <https://doi.org/10.1002/2013GL059059>, 2014.
- 1359 Tagliabue, A., Aumont, O., De'Ath, R., Dunne, J. P., Dutkiewicz, S., Galbraith, E., Misumi, K., Moore, J. K.,
1360 Ridgwell, A., Sherman, E., Stock, C., Vichi, M., Völker, C., and Yool, A.: How well do global ocean
1361 biogeochemistry models simulate dissolved iron distributions?, *Global Biogeochem. Cy.*, 30, 2,
1362 <https://doi.org/10.1002/2015GB005289>, 2016.
- 1363 Takeda, S., Kamarani, A., and Kawanobe, K.: Effects of nitrogen and iron enrichments on phytoplankton
1364 communities, *Mar. Chem.*, 50, 229–241, [https://doi.org/10.1016/0304-4203\(95\)00038-S](https://doi.org/10.1016/0304-4203(95)00038-S), 1995.
- 1365 Thushara, V., Vinayachandran, P. N. M., Matthews, A. J., Webber, B. G. M., and Queste, B. Y.: Vertical
1366 distribution of chlorophyll in dynamically distinct regions of the southern Bay of Bengal, *Biogeosciences*, 16,
1367 1447–1468, <https://doi.org/10.5194/bg-16-1447-2019>, 2019.
- 1368 [Twining, B. S., Rauschenberg, S., Morton, P. L., and Vogt, S.: Metal contents of phytoplankton and labile](https://doi.org/10.1016/j.pocean.2015.07.001)
1369 [particulate material in the North Atlantic Ocean, *Progr. Oceanogr.*, 137, 261–283,](https://doi.org/10.1016/j.pocean.2015.07.001)
1370 <https://doi.org/10.1016/j.pocean.2015.07.001>, 2015.
- 1371 Twining, B. S., Rauschenberg, S., Baer, S. E., Lomas, M. W., Martiny, A. C., and Antipova, O. M.: A nutrient
1372 limitation mosaic in the eastern tropical Indian Ocean, *Deep-Sea Res. Pt. II*, 166, 125–140,
1373 <https://doi.org/10.1016/j.dsr2.2019.05.001>, 2019.
- 1374 [Twining, B. S., Antipova, O., Chappell, P. D., Cohen, N. R., Jacquot, J. E., Mann, E. L., et al.: Taxonomic and](https://doi.org/10.1002/lol2.10179)
1375 [nutrient controls on phytoplankton iron quotas in the ocean, *Limnology and Oceanography Letters*, 6\(2\), 96–106,](https://doi.org/10.1002/lol2.10179)
1376 <https://doi.org/10.1002/lol2.10179>, 2021.
- 1377 Unger, D., Ittekkot, V., Schäfer, P., Tiemann, J., and Reschke, S.: Seasonality and interannual variability of
1378 particle fluxes to the deep Bay of Bengal: influence of riverine input and oceanographic processes, *Deep-Sea Res.*
1379 *Pt. II*, 50, 897–923, 2003.
- 1380 Vialard, J., Duvel, J. P., McPhaden, M. J., Bouruet-Aubertot, P., Ward, B., Key, E., Bourras, D., Weller, R.,
1381 Minnett, P., Weill, A., Cassou, C., Eymard, L., Fristedt, T., Basdevant, C., Dandonneau, Y., Duteil, O., Izumo,
1382 T., de Boyer Montégut, C., Masson, S., and Kennan, S.: Cirene: Air – Sea Interactions in the Seychelles – Chagos
1383 Thermocline Ridge Region, *B. Am. Meteor. Soc.*, 90, 45–62, <https://doi.org/10.1175/2008BAMS2499.1>, 2009.
- 1384 Vidya, P. J. and Prasanna Kumar, S.: Role of mesoscale eddies on the variability of biogenic flux in the northern
1385 and central Bay of Bengal, *J. Geophys. Res.-Oceans*, 118, 5760–5771, <https://doi.org/10.1002/jgrc.20423>, 2013.

- 1386 Vidya, P. J., Prasanna Kumar, S., Gauns, M., Verenkar, A., Unger, D., and Ramaswamy, V.: Influence of physical
1387 and biological processes on the seasonal cycle of biogenic flux in the equatorial Indian Ocean, *Biogeosciences*,
1388 10, 7493–7507, <https://doi.org/10.5194/bg-10-7493-2013>, 2013.
- 1389 Vinayachandran, P. N., Chauhan, P., Mohan, M., and Nayak, S.: Biological response of the sea around Sri Lanka
1390 to summer monsoon, *Geophys. Res. Lett.*, 31, L01302, <https://doi.org/10.1029/2003GL018533>, 2004.
- 1391 Vinayachandran, P. N., Shankar, D., Vernekar, S., Sandeep, K. K., Amol, P., Neema, C. P., and Chatterjee, A.: A
1392 summer monsoon pump to keep the Bay of Bengal salty, *Geophys. Res. Lett.*, 40, 1777–1782,
1393 <https://doi.org/10.1002/grl.50274>, 2013.
- 1394 Vu, H. and Sohrin, Y.: Diverse stoichiometry of dissolved trace metals in the Indian Ocean, *Sci. Rep.*, 3,
1395 doi:10.1038/srep01745,2013.
- 1396 Wang, S., Bailey, D., Lindsay, K., Moore, J. K., and Holland, M.: Impact of sea ice on the marine iron cycle and
1397 phytoplankton productivity, *Biogeosciences*, 11, 4713–4731, <https://doi.org/10.5194/bg-11-4713-2014>, 2014.
- 1398 Webber, B. G. M., Matthews, A. J., Vinayachandran, P. N., Neema, C. P., Sanchez-Franks, A., Vijith, V., Amol,
1399 P., and Baranowski, D. B.: The dynamics of the Southwest Monsoon current in 2016 from high-resolution in situ
1400 observations and models, *J. Phys. Oceanogr.*, 48, 2259–2282, <https://doi.org/10.1175/JPO-D-17-0215.1>, 2018.
- 1401 Wiggert, J. D., and Murtugudde, R. G.: The sensitivity of the Southwest Monsoon phytoplankton bloom to
1402 variations in aeolian iron deposition over the Arabian Sea, *J. Geophys. Res.*, 112, C05005,
1403 <https://doi.org/10.1029/2006JC003514>, 2007.
- 1404 ~~Witter, A., Lewis, B., and Luther, G. I.: Iron speciation in the Arabian Sea, *Deep Sea Res. II*, 47, 1517–1539,
1405 [doi:10.1016/S0967-0645\(99\)00152-6](https://doi.org/10.1016/S0967-0645(99)00152-6), 2000.~~
- 1406 Wyrтки, K.: An equatorial jet in the Indian Ocean, *Science*, 181, 262–264,
1407 <https://doi.org/10.1126/science.181.4096.262>, 1973.
- 1408 Xie, P. and Arkin, P. A.: Global precipitation: A 17-year monthly analysis based on gauge observations, satellite
1409 estimates, and numerical model outputs, *B. Am. Meteorol. Soc.*, 78, 2539–2558, [https://doi.org/10.1145/1520-0477\(1997\)078<2539:GPAYAMA>2.0.CO;2](https://doi.org/10.1145/1520-0477(1997)078<2539:GPAYAMA>2.0.CO;2), 1997.
- 1411 Yang, X., Zhao, C., Yang, Y., and Fan, H.: Long-term multi-source data analysis about the characteristics of
1412 aerosol optical properties and types over Australia, *Atmos. Chem. Phys.*, 21, 3803–3825,
1413 <https://doi.org/10.5194/acp-21-3803-2021>, 2021.
- 1414 ~~[Yoon, J.-E., Yoo, K.-C., Macdonald, A. M., Yoon, H.-I., Park, K.-T., Yang, E. J., Kim, H.-C., Lee, J. I., Lee, M.
1415 K., Jung, J., Park, J., Lee, J., Kim, S., Kim, S.-S., Kim, K., and Kim, I.-N.: Reviews and syntheses: Ocean iron
1416 fertilization experiments – past, present, and future looking to a future Korean Iron Fertilization Experiment in
1417 the Southern Ocean \(KIFES\) project, *Biogeosciences*, 15, 5847–5889, <https://doi.org/10.5194/bg-15-5847-2018>,
1418 \[2018\]\(https://doi.org/10.5194/bg-15-5847-2018\).](https://doi.org/10.5194/bg-15-5847-2018)~~

1419 Zhang, Y., Rossow, W. B., Lacis, A. A., Oinas, V., and Mishchenko, M. I.: Calculation of radiative fluxes from
1420 the surface to top of atmosphere based on ISCCP and other global data sets: Refinements of the radiative transfer
1421 model and the input data, *J. Geophys. Res.*, 109, D19105, <https://doi.org/10.1029/2003JD004457>, 2004.

1422